Investigation of Charge-Storage Mechanisms of Early-Transition-Metal Nitrides and Carbides as Electrodes for Electrochemical Capacitors

by

Priyanka Pande

A dissertation submitted in partial fulfillment
of the requirements for the degree of
Doctor of Philosophy
(Chemical Engineering)
in the University of Michigan
2013

Doctoral Committee:

       Professor Levi T. Thompson, Jr., Chair
       Professor Erdogan Gulari
       Assistant Professor Charles W. Monroe
       Professor James E. Penner-Hahn
       Emeritus Professor Paul G. Rasmussen

To my parents Vidhu and Lalit, my brother Kunal and my fiancé Vivek.

Acknowledgements

First, I would like to thank my advisor, Prof. Thompson for his support and guidance throughout my PhD research. He has not only been an advisor to me but a great mentor. During my time in the Thompson research group, I was given the freedom to think outside the box and develop new ideas. I greatly appreciate the open communication I could have with Prof. Thompson about my research and the time he has invested in making me a better researcher. I am grateful to him for giving me the opportunities to attend several conferences, where I had the opportunity to learn from experts in different areas of research from all over the world. The time I have spent in the Thompson research group has helped me grow as an individual and a lot of it due to the environment that Prof. Thompson has inculcated in the group.

Next, I would like to thank Prof. Rasmussen. Although I was not officially co-advised, Prof. Rasmussen is my second advisor. I really appreciate his guidance throughout my research. He provided a chemist's perspective to my research. The conversations I had with him helped me direct the project into a more fundamental study. I thank him for his help and support during the last four years. I have benefitted immensely from his "short-courses" in chemistry.

Also, I would like to thank members of my dissertation committee: Prof. Penner-Hahn, Prof. Monroe and Prof. Gulari. I am grateful to Prof. Penner-Hahn for his help and guidance with the X-ray absorption spectroscopy. His expertise and inputs on the experimental design and the data analysis were valuable to this research. I am thankful to Prof. Monroe for teaching me the fundamentals of electrochemistry and his guidance, especially during the initial phase of my research. I would like to thank Prof. Gulari for his critical feedback and thought-provoking discussions.

I would also like to acknowledge all the past and present Thompson group members with whom I had the wonderful opportunity to work: Dr. Neil Schweitzer, Dr. Adam Lausche, Dr. Joshua Schaidle, Dr. Peter Aurora, Dr. Richard Ezike, Dr. Jason Gaudet, Dr. Kanako Okada, Dr. Binay Prasad, Dr. Aaron Shinkle, Dr. Fan Shi, Dr. Xaiohui Chen, Dr. SangOK Choi, Dr. Mei Yu, Dr. Peng Wang, Gang Wang, Keliang Wang, Xiaodong Yu, Amin Bazyari, Gaowei Wang, Tapiwa Mushave, Joshua Grilly, Yuan Chen, Allison Franck, Ryan Franck, Brian Wyvratt, Adul Djire, Jonathan Kucharyson, Anisha Rehlan, Siu on Tung and Jee-Jay Chen. They are extremely talented group of individuals. Over the last five years, my interactions with them have added more breadth to my thought process. I would especially like to acknowledge Dr. Saemin Choi, for several discussions on energy-storage devices. Saemin has been my go-to person, whenever I needed anything in the lab. I really appreciate his help during my time in the Thompson research group. Also, I would like to thank the

Table of Contents

List of Figures

List of Tables

Chapter 1

Introduction

1.1   Motivation

The energy-storage requirements for various applications like the electric grid, transportation, manufacturing and portable electronics are quite diverse, with varied storage capacities and response times ranging from a few seconds to several days [1-7]. Table 1.1 summarizes the energy storage performance requirements for various applications.

Table 1.1   Energy storage requirements of various sectors [1-3].

Application	Stored Capacity	Discharge Period
Grid Leveling	10 MJ- 200 GJ	Seconds to Days
Power quality	0.1- 10 MJ	Seconds
Transport	2 GJ	Seconds to Days
Portable electronics	0.001- 0.1 MJ	Seconds to Days

At present, batteries are the principal energy storage devices used in most of these applications [1-5]. Batteries store electrical energy by converting it into chemical energy. These devices can have energy densities in excess of 100 $Whkg^{-1}$, however, due to kinetic and transport limitations, batteries have low power densities [1-5]. When batteries are cycled at high rates to meet pulse-power requirements, their lifetime and energy-storage capabilities are

significantly diminished due to loss of structural integrity of the electrodes caused by irreversible reactions [4]. To mitigate pulse-power loads, electrochemical capacitors could complement batteries in hybrid configurations [1-6].
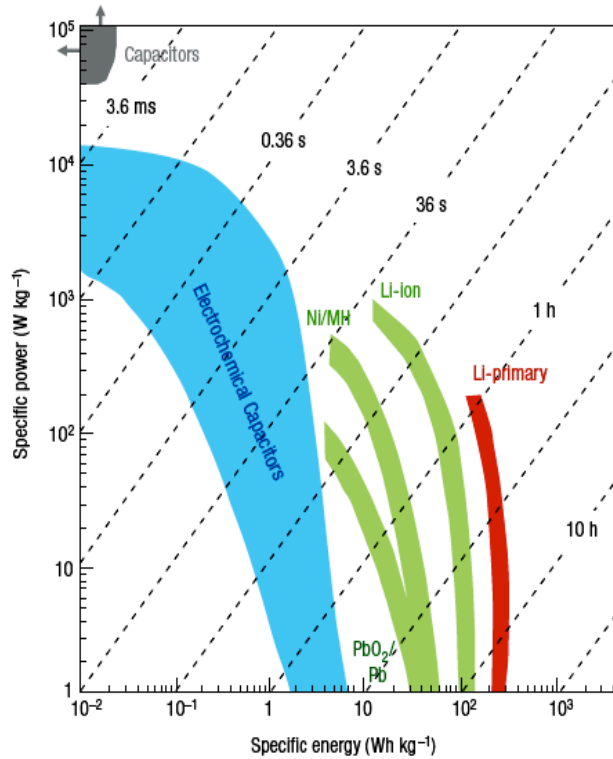
Figure 1.1 Comparison of power versus energy density characteristics of energy storage devices. Taken from [5].

Electrochemical capacitors (ECs), also known as supercapacitors or ultracapacitors, are a class of energy-storage devices that demonstrate high cycle life, high power density, and moderate energy density [1-5]. Figure 1.1 illustrates a comparison of the power and energy densities of various energy-storage devices [1-5]. In terms of performance, electrochemical capacitors fill the gap between batteries and conventional capacitors. Present state-of-the-art electrochemical capacitors are capable of handling short-term pulse-power

requirements limited to a few seconds [5]. To meet future requirements of longer pulse periods, ECs with higher energy densities will be needed [1-3, 5,6].

The energy stored (E) in an electrochemical capacitor scales as (1.1) [4]

$$E \approx \frac{1}{2}QV \approx \frac{1}{2}CV^2 \qquad (1.1)$$

where, Q is the charged stored, C is the capacitance and V is the operating voltage. The operating voltage of the system is dependent on the voltage window over which the electrodes and electrolytes are stable, while the capacitance or the charge stored is linked to the charge-storage mechanism. ECs can store charge by two mechanisms: (i) electrochemical double-layer formation, involving electrostatic charge separation of ions at the electrode-electrolyte interface and/or (ii) pseudocapacitance, involving fast, near-surface, redox reactions of the electrode materials with the electrolyte [4].

1.2 Electrochemical Double Layer Capacitors

In electrochemical double-layer capacitors (EDLCs), charge is stored through reversible electrolyte ion adsorption on the surface of the polarized electrode thus forming a 'double-layer' of opposite charges at the electrode-electrolyte interface [1-5]. This is a non-Faradaic charge storage process in that no electron transfer takes place and storage of electric charge is electrostatic [1-5]. The double layer capacitance is explained by the Gouy-Chapman-Stern model and is given equation 1.2 [4].

$$\frac{1}{C_{dl}} = \frac{1}{C_H} + \frac{1}{C_{diff}}$$

(1.2)

where C_{dl} is the overall double layer capacitance, C_H is the capacitance from the Helmholtz layer and the C_{diff} is the capacitance of the diffuse layer of electrolyte extending beyond the Helmholtz layer [4,7]. Figure 1.2 shows a schematic of the Gouy-Chapman-Stern double layer model [7].
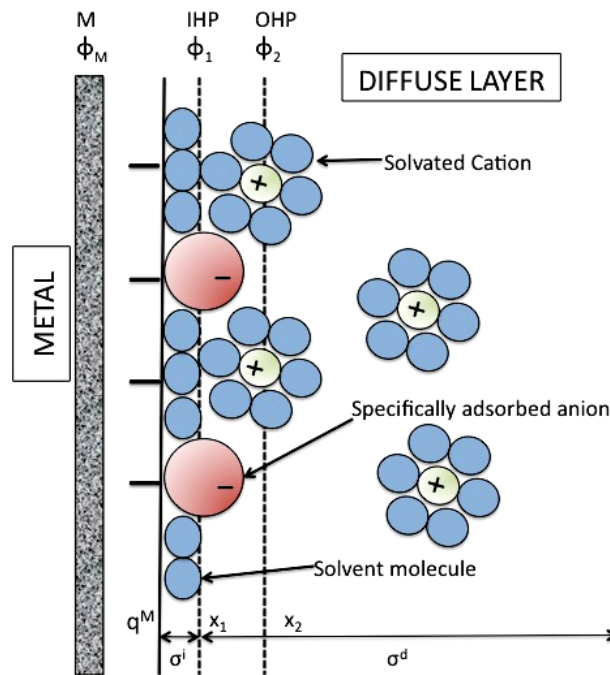
Figure 1.2 Schematic of the diffused double layer. IHP and OHP are the inner and the outer Helmholtz planes, M is the surface of the metal, and σ is the charge on each surface. Redrawn from [7].

The solution side of the double layer is thought to be made of several layers [4,7]. The layer closest to the electrode is called the inner layer, which contains specifically adsorbed solvent molecules or other ions or molecules. This layer is also referred to as the compact, Helmholtz, or Stern layer. The locus of the electrical centers of the specifically adsorbed species is called as the inner

Helmholtz plane (IHP), which is at distance x_1. The solvated ions can approach the electrode surface at a distance of x_2; the locus of the nearest solvated ions is called the outer Helmholtz plane (OHP). The interaction of these solvated ions with the electrode surface involves long-range electrostatic forces and is independent of their chemical properties. The region extending beyond the OHP into the bulk solution is called the diffuse layer. For concentrations greater than 0.01M the thickness of the diffuse layer is ~100 Å [7].

The Helmholtz capacitance C_H is given by equation 1.3.

$$C_H = \frac{A\varepsilon_0\varepsilon_r}{d} \tag{1.3}$$

ε_0 is the dielectric constant of vacuum, ε_r is the dielectric coefficient of the electrolyte, A is the area of the electrode accessible to the ions and d is the effective thickness of the double layer (x_1+x_2) in the electrolyte. According to the Helmholtz model, an increase in the accessible surface area of the electrodes will lead to higher capacitances [4,7]. The C_H is thought to be independent of polarization voltage, however at low electrolyte concentrations C_{diff} is thought to be dependent on applied potentials [7]. The C_H and C_{diff} are conjugate components of the overall double layer capacitance. The combined capacitance of the double-layer and the diffused layer varies from 15-50 μFcm^{-2} [4].

At present, commercially available ECs are based on double-layer capacitance and consist of high-surface-area-carbon electrodes with organic electrolyte solutions [1-6]. The surface areas of these carbon-based electrode

materials approach ~3000 m^2/g [5,6,8]. The electrolyte solution typically consists of an organic solvent like propylene carbonate or acetonitrile with a quaternary ammonium salt [1,4,5,6]. Most commercially available ECs use tetraethylammonium tertrafluoroborate in acetonitrile as the electrolyte solution [5]. The capacitances for EDLCs are typically 100-125 Fg^{-1} with voltage windows of nearly 3V [1,4,5,6]. In some cases ionic liquids have been used as electrolytes for EDLCs, with voltage windows approaching ~4V [8]. However, the capacitance of these systems is lower compared to EDLCs based on organic electrolyte solutions due to their large ion sizes, which reduce the accessible area for double-layer formation [10]. Figure 1.3 shows a typical rectangular cyclic voltammogram for an EDLC [5]. Despite wide operating voltages the energy density for EDLCs are limited to ~5 Whkg^{-1}, due to low capacitances [1-5].

The low capacitance and energy density of EDLCs is attributed to poor utilization of electrode area, as most of the surface area of carbon-based electrode is from micropores, which are not easily accessed by the large organic electrolyte ions [10]. In order to improve the energy densities, there are two possible approaches: (i) improvement of accessible surface area of carbon-based electrodes and/or (ii) development of more electrochemically stable electrolytes.
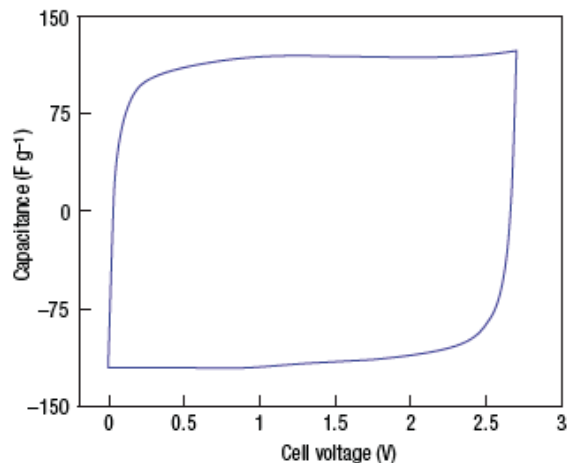
Figure 1.3 Cyclic Voltammogram of activated carbon in 1.5M tetraethylammonium terafluoroborate in acetonitrile at a scan rate of 20mVs[-1] [5].

1.3 Pseudocapacitors

In pseudocapacitors, capacitance originates from charge transfer processes, in addition to double-layer charge storage. The extent of charge transferred, ΔQ, between the electrode and electrolyte salt depends on the potential gradient, ΔV, created at the electrode-electrolyte interface [4]. These processes are limited by a finite quantity of active species in the electrolyte solution or on the surface site on the electrode surface. The pseudocapacitance, C_ϕ is characterized by the following equation (1.4) [4]

$$C_\phi = \frac{d(\Delta Q)}{d(\Delta V)} = \frac{dQ}{dV} \tag{1.4}$$

In pseudocapacitors, double-layer capacitance accounts for merely 5-10% of the total charge stored [4]. A number of pseudocapacitive materials have been reported including oxides of Ru, Mn, Mo, Fe, Co, Ni, V, Cu and Nb [4,11-20] and conducting polymers like polyaniline, polypyrrole, polythiophene and their derivatives [21-24].

7

Hydrous RuO_2 is the benchmark pseudocapacitive material with reports of capacitances up to 1300 Fg^{-1}; depending on the charge-discharge conditions [4,11,12] and energy densities in excess of 8 Whkg^{-1} [4].
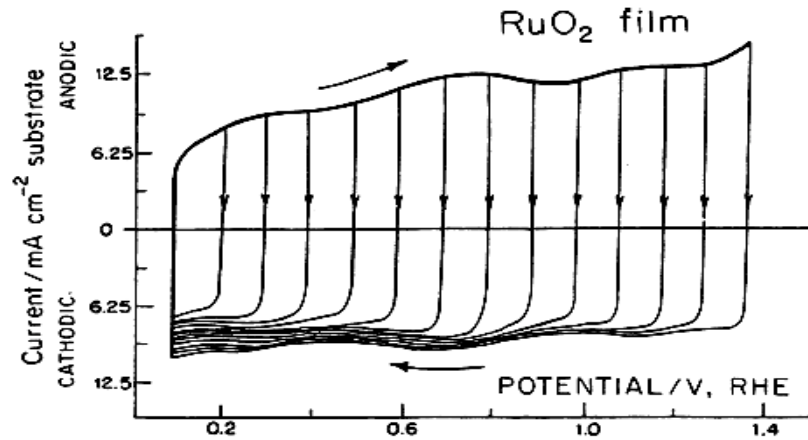
Figure 1.5 Cyclic voltammogram of RuO_2 film in 0.1M aqueous H_2SO_4, showing reversible 'mirror-image' redox behavior, scanned by increasing the potential window between 0.05V to 1.4V v/s RHE at a scan rate of 50 mVs^{-1} [10].

For hydrous RuO_2 the charge storage reaction is given by eq. 1.5:

$$RuO_2 + xH^+ + xe^- \leftrightarrow Ru_{2-x}(OH)_x \qquad (1.5)$$

where $0 \leq x \leq 2$. The continuous change in the oxidation state of Ru during proton insertion and removal which occurs over a window of about 1.4 V leads to charge storage and thus the pseudocapacitance [4]. This pseudocapacitance is almost an order of magnitude higher than the double-layer-charge storage observed in state of the art double-layer capacitors [4]. Figure 1.5 shows a cyclic voltammogram of RuO_2 in 0.1 M aqueous sulfuric acid [4]. Here the distinct peaks in the cyclic voltammogram can be attributed to a series of Ru oxidation states displayed (from Ru(II) to Ru(IV)). The mirror image oxidation and reduction curves suggest highly reversible redox processes [4]. Although hydrous RuO_2 is

attractive in terms of performance, the high cost of Ru limits its large-scale usage.
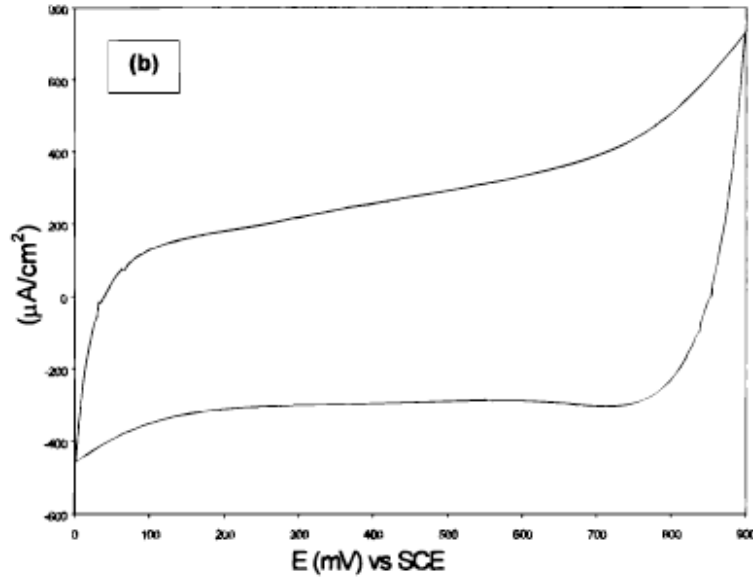
Figure 1.6 Cyclic voltammogram of electrodeposited MnO_2 in 0.1M Na_2SO_4 at a scan rate of 50mVs^{-1}, at room temperature, taken from [25].

MnO_2 is a less costly alternative to RuO_2 for supercapacitors. The capacitances for MnO_2 powders or micrometer-thick films are typically in the range of 150-220 Fg^{-1} in aqueous solutions of alkali metal (K, Na and Li) SO_4^{2-}, NO_3^- or Cl$^-$ salts [5,12,25]. Figure 1.6 shows a typical cyclic voltammogram of MnO_2 in 0.1M aqueous Na_2SO_4 [25]. While the cyclic voltammogram of MnO_2 is rectangular and seems similar to that of double-layer capacitors, high capacitances, in excess of 200 Fg^{-1}, have been attributed to pseudocapacitive charge storage, involving cation insertion. The reaction mechanism has been shown to follow [5].

$$MnO_2 + xM^+ + yH^+ + (x+y)e^- \leftrightarrow MnOOM_xH_y \tag{1.6}$$

Here M^+ is the K^+ or Na^+ or Li^+ electrolyte cation inserted into MnO_2. Ultra-thin MnO_2 films formed on metal current collectors have been reported to have capacitances near 1000 Fg^{-1} [12,25]. Due to the very low loadings, thin films are limited to micro-system applications and are not suitable for most large-scale industrial applications [12,26].

Although promising, oxides of Ru and Mn are not suitable for wide-spread application in ECs due to the high cost of Ru and poor electronic conductivity of MnO_2 (10^{-5} to 10^{-6} Scm^{-1}) [12]. Polymer-based pseudocapacitors are challenged by poor stabilities and very slow response times [5]. Exploitation of the pseudocapacitive mechanism would require development of low-cost electrode materials with high electronic conductivities and electrochemical stability.

1.4 Early Transition Metal Nitrides and Carbides

In the last decade there have been several investigations of the use of early transition metal nitrides and carbides as electrode materials in ECs [27-40]. These materials are formed by incorporating nitrogen or carbon into the interstitial sites of the parent metal lattice [42]. They combine properties of three different classes of materials: they are extremely refractory, like covalent solids; have high melting points, like ionic crystals; and are excellent heat and electronic conductors (Table 1.2), like metals [42]. The coexistence of these properties has been attributed to their unique electronic and structural characteristics [41-43].

Table 1.2 Conductivities of selected early transition metal nitrides and carbides compared to those of Ru_2O and Al.

Material	Conductivity[42] $\times 10^7$ $(\Omega m)^{-1}$
VN	0.11
VC	0.16
Mo_2N	0.5
Mo_2C	0.14
WN	1.1
WC	0.45
Ru_2O	0.002
Al	3.5

In 1973, Levy and Boudart demonstrated that early transition metal carbides have surface electronic properties similar to those of noble metals [41]. Oyama extended Levy and Boudarts' findings to early transition metal nitrides [43]. Since then, these materials have been tested for various thermocatalytic and electrocatalytic reactions either as catalysts or as active-catalyst supports. [42,44,47-51]. As catalytic applications require large availability of surface atoms, these applications have led to the development of various pathways to make high-surface-area carbides and nitrides in the range of 60- 200 m^2g^{-1} [42-51].

Early transition-metal-nitrides and carbides have been reported to exhibit pseudocapacitive behavior in aqueous electrolytes [27-40]. Vanadium Nitride (VN) has been characterized in aqueous KOH [28,29,31,33,37-39]; the highest capacitance observed has been 1340Fg^{-1} [29]. VN has also been characterized in aqueous NaCl [33], $NaNO_3$ [31] and H_2SO_4 [33,31]. Vanadium carbide (VC) has been investigated in aqueous KOH, with highest capacitance of 44Fg^{-1} [28]. Molybdenum Nitride [Mo_xN or Mo_2N] has been studied in aqueous H_2SO_4 [27,28,35,36,39] and aqueous KOH [30]. The highest capacitance reported for

Mo_2N has been $172 Fg^{-1}$ in aqueous H_2SO_4 [35]. Niobium nitride (NbN) has been investigated in aqueous KOH [30,37], with highest capacitance reported as $73 Fg^{-1}$ [30]. Titanium nitride (TiN) has been characterized in aqueous KOH [32,37] with the highest capacitance of $238 Fg^{-1}$ [32]. Tungsten nitride (WN) has been studied in aqueous KOH [39,40]. Highest capacitance reported for WN in aqueous KOH was $30\ Fg^{-1}$ [40]. Tungsten carbide (WC) was characterized in aqueous H_2SO_4 [28,39], with highest capacitance of $17\ Fg^{-1}$ [28].

While there are several reports on stability assessments of and capacitance measurements for these materials, there are few reports characterizing their charge storage mechanisms [27,29]. The charge storage mechanisms for VN in KOH and Mo_xN in H_2SO_4, have been investigated by Choi et al. [29] and Liu et al. [27], respectively.

Choi et al. used results from post-cycling Fourier-transform infrared (FTIR) spectroscopy and x-ray photoelectron spectroscopy (XPS) to propose the charge storage mechanism for VN in aqueous KOH electrolyte solution. The figure 1.7 shows the characterization results obtained by Choi et al. [29], before and after cyclic voltammetry experiments. From figure 1.7 (a), they suggested a presence of an amorphous vanadium oxide layer, attributing it to the FTIR absorption bands at 970 (V=O) and 792 (V-O) cm^{-1}. For VN immersed in KOH in additional peaks 3000- 3500 cm^{-1} were observed, which were attributed to hydroxyl ions. For the VN electrode after 10 cycles, they saw a "free" –OH stretching peak around 3535 cm^{-1}, while the peak at 3423 cm^{-1} was assigned to hydrogen bound –OH. The peak at 3047 cm^{-1} was assigned to $VO(OH)_2$.
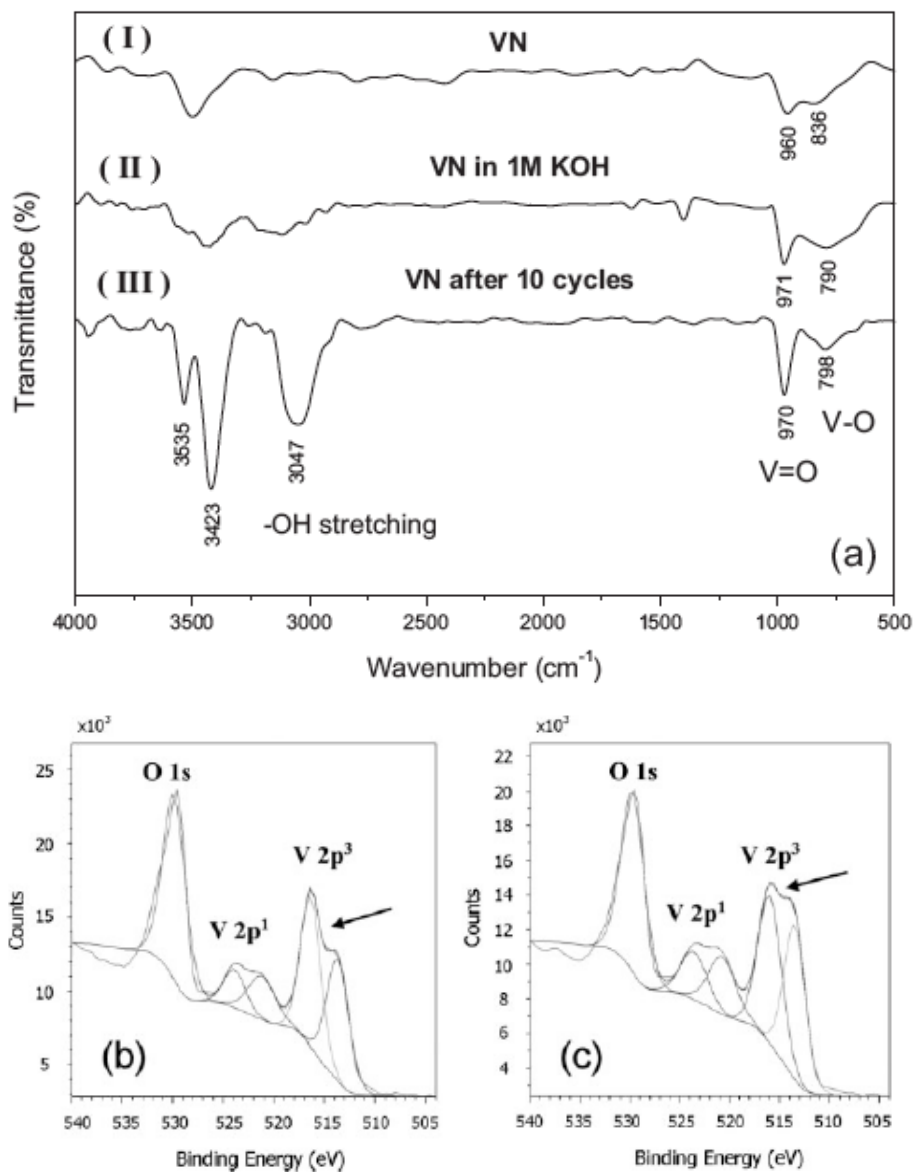
Figure 1.7 (a) Fourier-transform infrared spectra (FTIR) for (I) VN crystals, (II) VN crystals immersed in 1M KOH and (III) After 10 cycles. (b) VN electrode before cycling, (c) VN electrode after 200 cycles. Taken from [29].

From the XPS characterization results in figure 1.7 (b) and (c), Choi et. al. speculated that the surface oxide film showed presence of V_2O_5 before cycling, based on the binding energy of the $V2p^3$ peak. The post cycling XPS results suggested reduction of vanadium, presence of VO_2 or V_2O_3 was suggested.

These results led them to propose a mechanism involving a redox reaction of the oxy-nitride passivation layer with OH⁻ as well as double-layer charging given by equation (1.7) [29]

$$VN_X O_Y + OH^- \leftrightarrow VN_X O_Y \parallel OH^- + VN_X O_Y - OH \qquad (1.7)$$

While this study provides insights into the changes of the VN surface after cycling, the specific charge transfer events occurring on VN during charge storage could not be identified due to *ex situ* characterization techniques employed in this investigation.

The charge storage mechanism for Mo_2N in aqueous H_2SO_4 was investigated by Liu et al. [27]. They saw that the rest potential of the system decreases linearly with the increase in pH. The slope of this relationship was $\frac{\Delta E}{\Delta pH} = -60mV$, similar to the reversible hydrogen electrode. As pH is a measure of H^+ activity, this led them to speculate that a proton and an electron participate in the charge storage reaction for Mo_xN in H_2SO_4. They proposed two charge storage mechanisms, one involving protons with the reduction of Mo (equation 1.8) and the second and the other involving hydrolyzed Mo (equation 1.9) [14].

$$Mo^{3+}N^{3-} + H^+ + e^- \leftrightarrow Mo^{2+} + NH^{2-} \qquad (1.8)$$

$$Mo^{3+}O^{2-}OH^- + H^+ + e^- \leftrightarrow Mo^{2+}(OH^-)_2 \qquad (1.9)$$
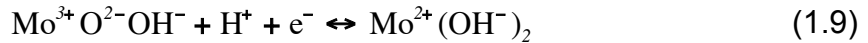
This report attributed pseudocapacitive activity observed on Mo_xN to H^+ [27], however no characterization of the redox reactions on material was performed.

Early transition metal nitrides and carbides are promising candidates for use in ECs, due to their high electronic conductivities, surface areas,

electrochemical stabilities and capacitances. Further development of these electrode materials will benefit from a better understanding of how changes occur in the electrode material during the charge-transfer process.

1.5   Research Goal and Organization of Text

The goal of the research described in this dissertation is to define charge storage mechanisms for early transition-metal-nitride and carbide as electrochemical capacitor electrodes. The specific objectives set to achieve this goal are as follows:

i. Synthesize and characterize high- surface area early transition metal carbides and nitride materials

ii. Identify promising systems in terms of operating voltage window and capacitance

iii. Establish charge-storage reactions of the form:

$$\text{Reduction} \leftrightarrow \text{Oxidation} + e^-$$

by developing relations between three key components: electrolyte, electrode material and the electrons transferred as a result of the electrode-electrolyte interaction.

The text in this dissertation is organized into five chapters, of which this introduction is the first. A brief description of the remaining chapters is provided below:

Chapter 2: Material Synthesis and Characterization

This chapter discusses conditions used to synthesize nitrides and carbides of V, Mo and W. Physical characterization of the materials was performed using X-ray diffraction to establish crystal structure and N_2 physisorption to quantify surface-area. Electrochemical characterization was performed in aqueous electrolytes using cyclic voltammetry. Promising electrode-electrolyte systems were identified.

Chapter 3: Investigation of Charge Storage Mechanism

The focus of this chapter is to define redox reactions involved in pseudocapacitive charge storage of Mo_2N in H_2SO_4 and VN in KOH, the most promising system identified in chapter 2. An electrochemical reaction can be divided into three main components: (i) electrolyte ions involved in the reaction, (ii) electrons transferred from the circuit to the electrode during charge and vice versa during discharge and (iii) changes in the electrode material during charge storage.

The electrolyte ions participating in the charge storage reaction were identified by a series of ion isolation and substitution cyclic voltammetry experiments. The electron count was established by using a Nernstian relationship to relate the rest potential to the active ion concentration. Finally, changes in the electrode material were characterized using *in-situ* x-ray

absorption spectroscopy. Charge-storage redox reactions consistent with these results are proposed.

Chapter 4: Role of Solvent in Charge Storage Mechanism

In this chapter the possibility of using a non-aqueous electrolyte solution with active electrolyte ions is explored with the aim of achieving pseudocapacitive charge storage similar to in aqueous systems. VN in $[(C_2H_5)_4N]OH$ in acetonitrile solvent was used as the test system. Non-aqueous electrolytes have wider voltage windows compared to water. As the energy density of the supercapacitors varies as squared of the voltage, pseudocapacitive activity accompanied by a wide voltage window could greatly enhance the overall energy density of supercapacitor devices based on early transition metal nitrides.

Chapter 5: Summary, Conclusions, Limitations and Future Work

This chapter provides a summary of results and identifies the limitations of this research. Future experiments to mitigate the limitations of the current work have been proposed and a roadmap for development of prototype devices based on early transition metal nitrides and carbides has been discussed.

1.6   References:

1. M. S. Whittingham, Proceedings of IEEE, 100 (2012), 1518-1534.

2. D. R. Rolison, L. F. Nazar, MRS Bulletin, 36 (2011), 486-493.

3. P. J. Hall, E. J. Bain, Energy Policy, 36 (2008) 4352- 4355.

4. B.E. Conway, Electrochemical Supercapacitors; Kluwer Academic/ Plenum Publishers, (1999).

5. P. Simon, Y. Gogotsi, Nature Materials, 7 (2008), 845-854.

6. D. Cericola, R. Kötz, Electrochimica Acta 72 (2012) 1.

7. Bard, Allen. J.; Faulkner, Larry. R.; Electrochemical Methods 2nd Edition, John Wiley & Sons, inc., (2001).

8. Y. Zhu, S. Murali, M. D. Stoller, K. J. Ganesh, W. Cai, P. J. Ferreira, A. Pirkle, R. M. Wallace, K. A. Cychosz,3 M. Thommes, D. Su, E. A. Stach, R. S. Ruoff, Science, 332, (2011) 1537.

9. A. Lewandowski, M. Galin´ski, J. Phys. Chem. Solids, 65 (2004) 281.

10. C. Largeot, C. Portet, J. Chmiola, P.-L. Taberna, Y. Gogotsi, P. Simon, J. Am. Chem. Soc. 2008, 130, 2730.

11. C.-C. Hu, T.-W. Tsou, Electrochem. Commun. 4 (2002) 105.

12. C. Xu, F. Kang, B. Li, H. Du, J. Mater. Res. 25 (8) (2010) 1421.

13. M. Toupin, T. Brousse, D. Bélanger, Chem. Mater. 16 (16) (2004) 3184.

14. V. S. Saji, C.-W. Lee, ,ChemSusChem, 5, (2012) 1146 – 1161.

15. M. Nasibi, M. A. Golozar, G. Rashed, Mater. Chem. Phys., 139 (2013) 12.

16. H. Wang, Hernan S. Casalongue, Y. Liang, H. Dai, J. Am. Chem. Soc. 132 (2010), 7472.

17. J. W. Kim, V. Augustyn, B. Dunn, Adv. Energy Mater. 2, (2012), 141.

18. K.C. Liu, M. A. Anderson, J. Electrochem. Soc.,143, 1, (1996) 125.

19. C. Lin, A. Ritter, B.N. Popov, J. Electrochem. Soc. 145, 12, (1998) 4097.

20. A.M. Engstrom, F.M. Doyle, J. Power Sources, 228 (2013) 120.

21. A. Rudge, J. Davey, I. Raistrick, S. Gottesfeld, J. Power Sources, 47 (1994) 189.

22. L. Groenendaal, F. Jonas, D. Freitag, H. Pielartzik, J. R. Reynolds, Adv. Mater. 12, 7 (2000) 481.

23. E. Frackowiak, V. Khomenko, K. Jurewicz, K. Lota, F. B´eguin, J. Power Sources, 153 (2006) 413.

24. A. Rudge, J. Davey, I. Raistrick, S. Gottesfeld, J. P. Ferraris, Electrochimica Acta, 39, 2 (1994) 273.

25. S.-C. Pang, M. A. Anderson, T. W. Chapman, J. Electrochem. Soc. 147, 2 (2000) 444.

26. Y. Gogotsi, P. Simon, Science 334 (2011) 917.

27. T.-C Liu, W.G. Pell, B.E. Conway, J. Electrochem. Soc. 145 (6) (1998) 1882.

28. M.R. Wixom, D.J. Tarnowski, J.M. Parker, J.Q. Lee, P.-L. Chen, I. Song, L.T.Thompson, Mat. Res. Soc. Symp. Proc. 496, Boston, 1-5 Dec., 1997, (1998) 643.

29. D. Choi, G.E. Blomgreen, P.N. Kumta, Adv. Mater. 18 (2006) 1178.

30. D. Choi, P.N. Kumta, J. Am. Ceram. Soc., 94, 8 (2011) 2371.

31. F. Cheng, C. Hu, D. Shu, H Chen, J. Zhang, S. Tang. D.E. Finlow, Mater. Chem. Phy. 131 (2011) 268.

32. D. Choi, P.N. Kumta, J. Electrochem. Soc. 153, 12 (2006) A2298.

33. A. M. Glushenkov, D Hulicova-Jurcakova, D. Llewellyn, G. Q. Lu, Y. Chen, Chem. Mater., 22 (2010) 914.

34. X. Zhou, C. Shang, S. Dong, X. Chen, P. Han, L. Li, J. Yao, Z. Liu, H. Xu, Y. Zhu, G. Cui, Appl. Mater. Interfaces, 3 (2011) 3058.

35. X.-L. Li, Y. Xing, H. Wang, H.-L. Wang, W. Wang, X. Chen, Trans. Nonferrous Met. Soc. China, 19 (2000) 620.

36. S. L. Roberson, D. Finello, R. F. Davis, J. Appl. Electrochem. 29 (1999) 75.

37. R. Lucio Portoa, R. Frappiera, J.B. Ducrosa, C. Auchera, H. Mosquedaa, S. Chenub, B. Chavillonb, F. Tessierb, F. Cheviréb, T. Broussea, Electrochimica Acta 82 (2012) 257.

38. D. Shu, C. Lv, F. Cheng, C. He, K. Yang, J. Nan, L. Long, Int. J. Electrochem. Sci., 8 (2013) 1209.

39. P.Pande, P.G. Rasmussen, L.T. Thompson, J. Power Sources, 207 (2012) 212.

40. D. Choi, P.N. Kumta, J. Am. Ceram. Soc., 90,10 (2007) 3113.

41. Levy, R. B.; Boudart, M.; Science 181 (1973) 547.

42. S.T. Oyama, The Chemistry of Transition-metal Carbides and Nitrides, Chapman and Hall Publisher, 1996.

43. S.T. Oyama, Catal. Today 15 (1992) 179.

44. J.B. Claridge, A.P.E. York, A.J. Brungs, M.L.H. Green, Chem. Mater 12 (1) (2000) 132.

45. R. Kapoor, S.T. Oyama, J. Solid State Chem. 99 (1992) 303.

46. J.A. Schaidle, A.C. Lausche, L.T. Thompson, J. Catal. 272 (2010) 235.

47. L. Volpe, M. Boudart, J. Solid State Chem. 59 (1985) 332.

48. J.G. Chen, Chem. Rev. 96, 4 (1996) 1477.

49. S. Ramanathan, St. T. Oyama, J. Phys. Chem. 99, 44 (1995) 16355.

50. D. J. Ham, J. S. Lee, Energies, 2 (2009) 873.

51. H. Zhong, H. Zjang, G. Liu, Y. Liang, J. Hu, B. Yi, Electrochem. Comm., 8, 5 (2006) 707.

Chapter 2

Materials Synthesis and Characterization

2.1 Introduction

Early transition-metal-nitrides and carbides are interstitial compounds, formed by the incorporation of nitrogen or carbon, respectively, into the metal lattice [1]. These materials adopt simple crystalline structures, with metal atoms forming lattices of face centered cubic (*fcc*), hexagonal close packed (*hcp*), simple hexagonal (*hex*) structures, the non-metals (nitrogen or carbon) occupy the interstitial sites between the metal atoms [1-4]. Figure 2.1 shows structures of common metal nitrides and carbides.

• = *Carbon / Nitrogen*   ○ = *Transition Metal*
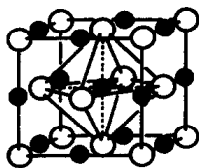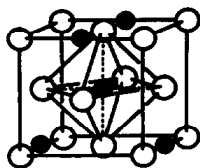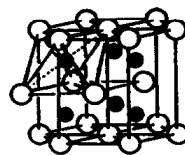
| Face centered cubic | | Hexagonal closed packed | Simple hexagonal |

TiC, VC, NbC $\gamma-Mo_2N,\ \beta-W_2N,\ Re_2N$ $\beta-Mo_2C,\ W_2C,\ Re_2C$ WC, MoC
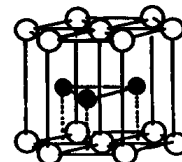
TiN, VN, NbN $^{\cdot}\alpha-MoC_{1-x},\ \beta-WC_{1-x}^{\cdot}$ $\delta-WN$

Figure 2.1 Crystal structures of early transition metal carbides and nitrides [3].

The Hägg rule explains the geometric factor determining the structure of these materials [4]. The Hägg rule proposes simple crystal structures (*fcc, hcp, hex*) will be formed if the ratio of hard-ball atomic radii of non-metal to metal is less than 0.59 [4]. The ratio of hard-ball atomic radii of selected metals with carbon and nitrogen are listed in Table 2.1.

Table 2.1 Solute (N or C) to solvent (Mo or V or W) hard sphere radii ratios of Early Transition metal nitride and carbide systems [4]**.**

System	Non-metal Radius/ Metal radius
Mo-C	0.56
Mo-N	0.52
V-C	0.58
V-N	0.53
W-C	0.55
W-N	0.49

The crystalline structures of nitrides and carbides are often different from those of parent metals. For example, Mo metal is *bcc*, while Mo_2C is *hcp* and Mo_2N is f*cc*. Similarly, vanadium metal is *bcc* while VN and VC are *fcc*. This change in the parent-metal structure has been attributed to the electronic factor explained by the Engel-Brewer theory. This theory proposes that the crystal structure of a material depends on the number of *sp* valence electrons per atom (e/a). When e/a= 1-1.5 *bcc* structures are formed, e/a is 1.7-2.1 *hcp* structure and when e/a is 2.5-3 *fcc* structure is preferred [1]. When early transition metal nitrides and carbides are formed the non-metal *s* and p orbital interact with the

spd band of the metal, thus changing the *sp* electron count and the structure of the parent metal [1].

Several methods exist for nitride or carbide synthesis, which start with pure metals, metal chlorides or metal oxides [1,2]. The most common approach for the synthesis of high-surface-area materials ls has been from inexpensive metal-oxide precursors [7-10]. In our group, a temperature programmed reaction method is used for nitride and carbide synthesis [5-11]

2.2   Materials Synthesis Procedure

High-surface-area V, Mo and W carbides and nitrides were synthesized from their respective precursors using the temperature-programmed-reaction method.   A quartz tube reactor was used, within which the precursor was supported on a quartz wool plug. The quartz-tube reactor was loaded into a vertical furnace. A schematic of the synthesis reactor is shown in figure 2.2 [11]. In order to make consistent batches of materials, the particle size of the precursors was in the range of 125- 250 μm prior to nitridation or carburization. The carbides were synthesized with 15% CH_4/H_2 gas mixture and the nitrides were synthesized with anhydrous NH_3 gas. The conditions are summarized in Table 1. After the synthesis, the materials were quenched to room temperature (RT) under the reaction gas and then passivated in a controlled manner under the flow of 1% O_2/He gas mixture for at least 5 h.
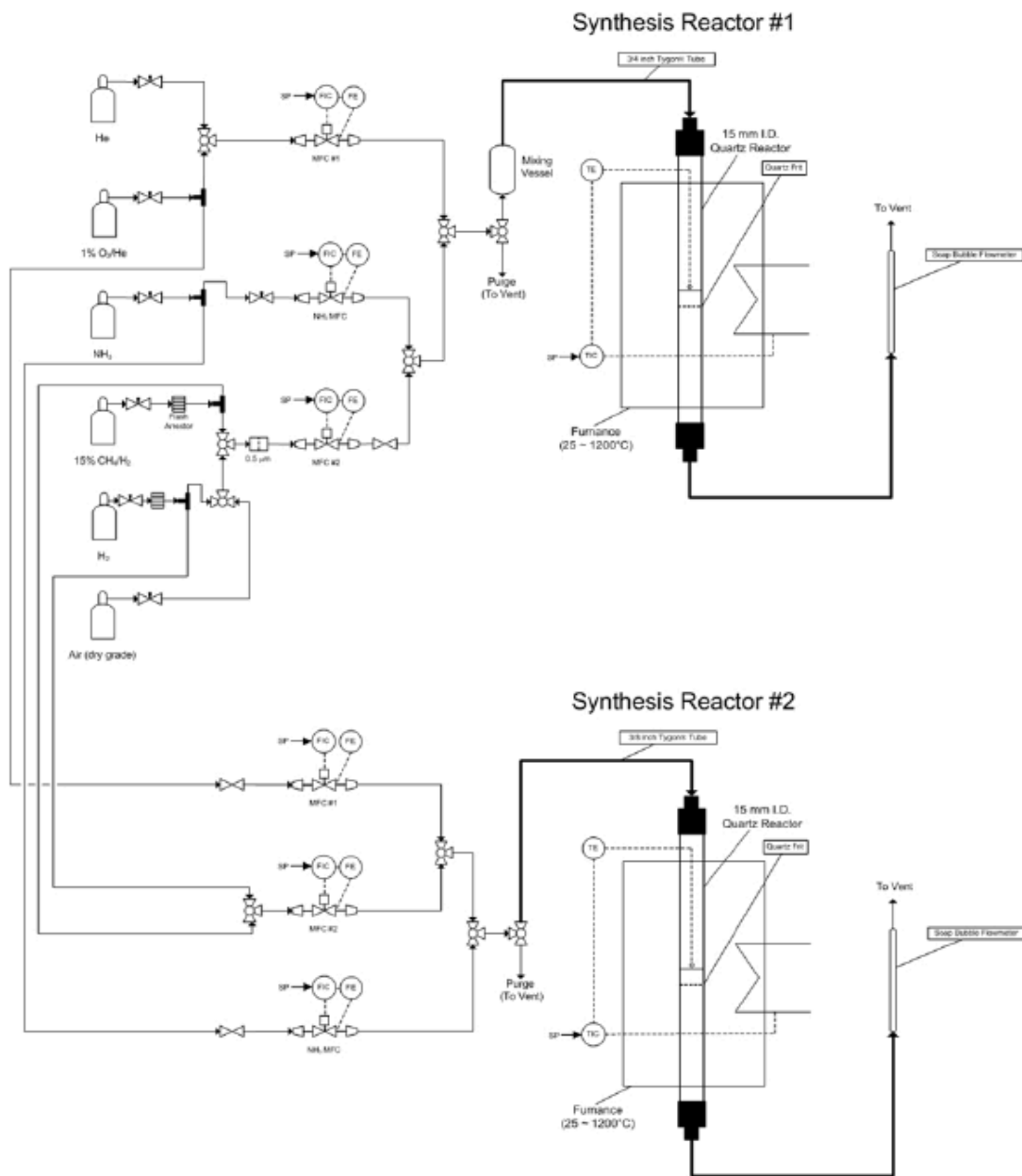
Figure 2.2 Schematic of reactor system used in synthesis of nitrides and carbides of Mo, V and W. Taken from [11].

Table 2.2 Summary of Temperature Programmed Synthesis for Early Transition Metal Nitrides and Carbides

Materials	Precursor	Gas Flow Rate ml min^{-1}	Temperature Program	Ref.
VC	0.4g V_2O_5 (99.99%, Sigma Aldrich)	400	RT to 157°C @ 8°Cmin^{-1} 157°C to 987°C @ 2°Cmin^{-1} Soak @ 987°C for 1hr	7
VN	0.5g V_2O_5 (99.99%, Sigma Aldrich)	1200	RT to 750°C @ 5°Cmin^{-1} Soak @ 750°C for 1hr	8
Mo_2C	1.3g $(NH_4)_6Mo_7O_{24}.4H_2O$ (81- 83% MoO_3, Alfa Aesar)	400	RT to 350°C @ 10°Cmin^{-1} in pure H_2. 350°C to 590°C @ 0.33°Cmin^{-1} Soak @ 590°C for 2hr	9
Mo_2N	1.5g $(NH_4)_6Mo_7O_{24}.4H_2O$ (81- 83% MoO_3, Alfa Aesar)	400	RT to 350°C @ 10°Cmin^{-1} 350°C to 450°C @ 0.66°Cmin^{-1} 450°C to 700°C @ 1.66°Cmin^{-1} Soak @ 700°C for 1hr	10
W_2C	1.1g WO_3 (99.99%, Alfa Aesar)	250	RT to 200°C @ 10°Cmin^{-1} 200°C to 650°C @ 1°Cmin^{-1} Soak @ 650°C for 5 hr	7
W_2N	1.3g WO_3 (99.99%, Alfa Aesar)	360	RT to 270°C @ 12°Cmin^{-1} 270°C to 560°C @ 0.5°Cmin^{-1} Soak @ 560°C for 16min	7

2.3   Materials Characterization

2.3.1   Physical Characterization

X-ray Diffraction Analysis (XRD)

XRD is a bulk characterization technique. When the incident X-rays interact with the atomic planes of the material, they disperse and interfere with one another, in the phenomenon called X-ray diffraction. XRD patterns show relative intensities of diffracted x-rays versus diffraction angle. Based on the

crystal structure of the material, the XRD pattern of the material exhibits peaks over a range of diffraction angles. These peak angles correspond to the various crystal planes in the material, and thus can be used to determine crystal structures and the crystallite size [12].

For the materials studied in this work, XRD was performed with a Rigaku Miniflex Diffractometer and Cu K_α (λ= 0.15404 nm) source. The samples were powdered and loaded on a glass sample holder. The XRD was carried out at a scan rate of $5.0^\circ min^{-1}$ with a step size of 0.1° over a 2θ range from 10° to 90°. The software used for peak identification was JADE 9.0, which has the International Centre for Diffraction Database built-in for phase identification. JADE matched the measured spectra to the database to obtain the chemical composition of the material.

N_2 physisorption: Brunauer-Emmett-Teller (BET) Surface Area Analysis

Brunauer, Emmett and Teller developed a relationship for multilayer adsorption of gases on the surface of a material. BET theory assumes that the gas molecules physically adsorb on the sample in compact, surface-covering layers and that distict adsorbed layer do not interact. This theory relates the adsorbed volume of the gas on the sample, v, to the equilibrium and saturation pressure of the gas, p and p_o, respectively. The BET equation (2.1) is shown below.

$$\frac{p}{v[p_o - p]} = \frac{c-1}{v_m c}\left(\frac{p}{p_o}\right) + \frac{1}{v_m c}$$

Here v_m is the volume of gas adsorbded in one monolayer and c is a constant. A plot of $\dfrac{p}{v[p_o - p]}$ versus $\left(\dfrac{p}{p_o}\right)$ is linear between relative pressures of 0.05 and 0.35. By fitting a line to this region v_m can be obtained from the slope and the y-intercept. The number of gas molecules adsorbing can be calculated from v_m. The surface area of the material is estimated by multiplying this number to the area coververd by a single gas molecule.

In this study, BET surface area of the materials was measured by N_2 physisorption using a Micromeritic ASAP 2010 analyzer. Approximately 0.1g of material was analyzed at a time. The materials were degassed at 350 °C under vacuum for 8 h, prior to surface area measurements. After degassing, the sample was moved to the analysis chamber. The analysis chamber was cooled to 77K with liquid N_2.

2.3.2 Electrochemical Characterization

Based on the previous studies exploring suitability of early transition-metal-nitrides and carbides as EC electrodes, aqueous electrolytic solutions of KOH and H_2SO_4 were chosen to establish electrochemical stability and measure capacitance of early transition metal nitrides and carbides [5,6, 13]. The following systems tested were: VN, VC, Mo_2C, Mo_2N, W_2C and W_2N in aqueous KOH (Alfa Aesar) and H_2SO_4 (99.999%, Sigma Aldrich). The electrolytic solutions

were 1M or 0.1M KOH and 0.5M or 0.1M H_2SO_4 prepared with ultrapure water (18.2 MΩ cm, Millipore Milli-Q Advantage A10). Cyclic voltammetry was used to determine the stable operating voltage window and also to measure the capacitance of the stable systems.

Cyclic Voltammetry:
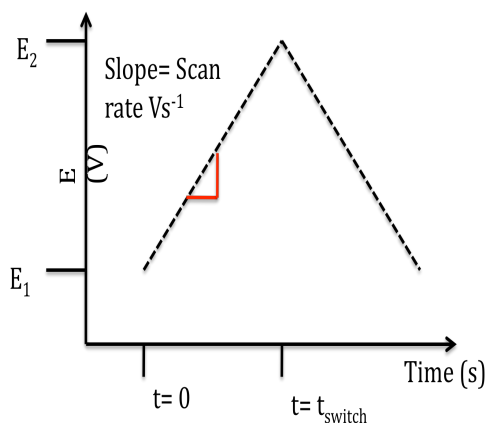
Figure 2.3 Potential waveform applied to the working electrode in the cyclic voltammetry experiment [14].

In cyclic voltammetry (CV), the current response of the working electrode (WE)− the material of interest− is recorded as a function of applied voltage. This generates a current versus voltage plot called the 'cyclic voltammogram', whose characteristic shape varies with the scan rate and voltage window [14]. In CV the voltage waveform is applied to the WE as shown in figure 2.3. The potential of the working electrode is initially set at E_1 and is linearly increased at a constant scan rate to E_2. The potential of the electrode is then reversed and scanned back to the original value. The potentials E_1 and E_2 are selected such that the redox reactions of interest occur within the potential window of (E_1-E_2) [14].

For this study, The CV experiments are carried out in a three-electrode apparatus, which consists of a working electrode (WE), a counter or current collector electrode (CE) and a reference electrode (RE). The potential of the WE is measured with respect to a RE chosen to be reversible with respect to a species in solution and therefore exhibit a stable standard potential. The current response of the WE is recorded with respect to a CE. The geometric area of the CE is much larger than the area than the WE, to avoid any resistive limitation to the WE current when measured versus the CE. A schematic of a typical three-electrode apparatus used in CV experiments is shown in figure 2.4. This cell is made of quartz. The WE and RE chambers interact with each other through a luggin capillary, while the chemistry occurring at the CE is isolated by barrier to the flow of ions to the WE chamber by a glass frit. An inlet to an inert gas line is provided in the WE chamber on order to deaerate the electrolyte solution prior to the experiments and to maintain an inert environment during the tests.
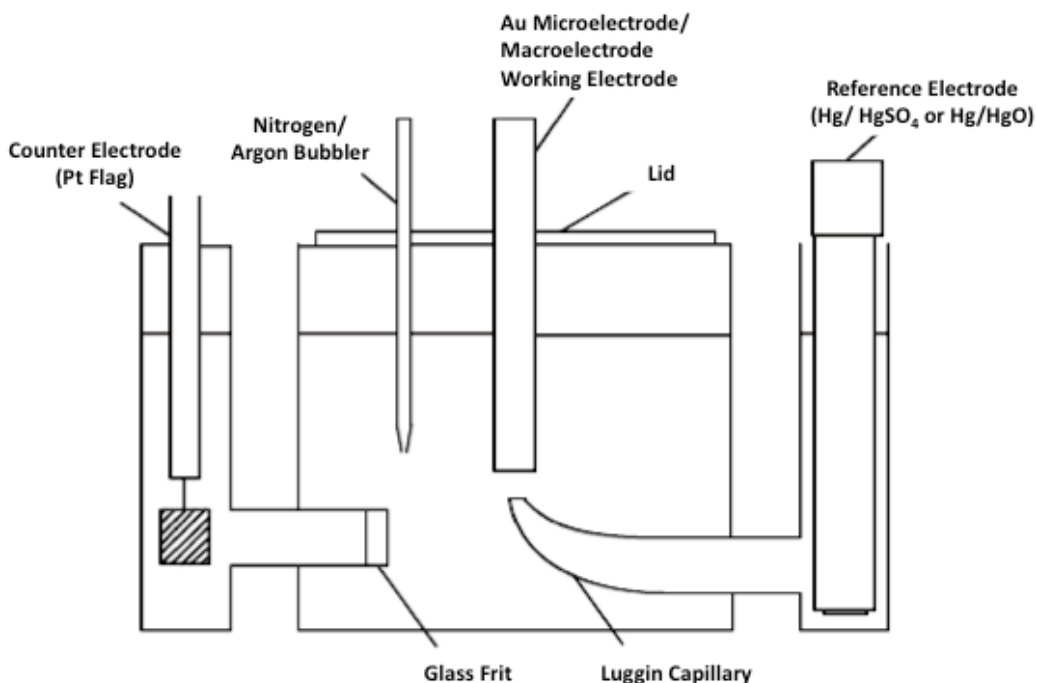
Figure 2.4 Schematic of a quartz three-electrode cell showing the central working electrode chamber and the reference and counter electrode chambers. The luggin capillary connects the working and the reference electrode chambers. The counter electrode chamber is isolated via a porous glass frit.

Materials and Methods:

An AUTOLAB PGSTAT302N potentiostat was used for electrochemical characterization of the early transition metal-nitrides and carbides. A platinum flag (99.99%, Alfa Aesar) was used as the CE, while Hg|HgSO$_4$ (Saturated. K$_2$SO$_4$, Radiometer Analytical) and Hg|HgO (0.1M KOH, Radiometer Analytical) were used as the REs in aqueous H$_2$SO$_4$ and aqueous KOH solutions respectively. Prior to the experiments, the aqueous electrolytic solutions were deaerated by N$_2$ (99.998% with an oxygen trap) for at least 20 min. A N$_2$ blanket was maintained in the WE chamber throughout the experiments.

The electrochemical stability assessment was carried out using an Au microelectrode as the WE in 0.5M H$_2$SO$_4$ and 1M KOH electrolyte solutions. The

Au microelectrodes were polished prior to each experiment using 15μm, 6μm and 0.1μm grit silicon carbide sand papers sequentially. The active-material powders were supported on the Au microelectrode by abrasive adhesion. The advantage of using microelectrodes is that very small quantities of materials are required for the test and the pure material can be characterized without binders or additives. Each material was cycled at a scan rate of 50mVs^{-1} for 100 cycles within a potential window that was expanded in a step-wise fashion by 0.1 V on both anodic and cathodic sides until the material showed evidence of instability or decomposition of the electrolyte. The experiments were performed at room temperature.

Capacitance measurements for the stable electrode-electrolyte systems combinations were carried out with 0.1M electrolytic solutions. The capacitances were measured on macroelectrodes. These were used instead of the microelectrodes to allow more precise measurement of the quantity of active material tested. The macroelectrodes were prepared by coating a slurry containing 80% active material, 10% graphite (Timcal KS-4 or Super P Li) and 10% polyvinylidene fluoride (Kynar) by mass, in N-methylpyrrolidinone (Alfa Aesar) solvent on a Ti foil (99.97%, Alfa Aesar, 0.127mm) and then drying the film in vacuum at 80 °C for 8 hours. Prior to the coating, the Ti foil was cut in to 1cm X 2.5cm sized strips. These strips were cleaned by sequential sonication (sonicatior: Cole Palmer H_2O Bath, ¾ Gal) in acetone, ethanol and ultrapure water, for 10 min each. This procedure ensured there were no surface contaminants. After sonication, the Ti strips were dried in the glassware oven for

at least 2h. Each Ti strip was weighed prior to coating. The slurry was coated on both sides of the Ti strip using a spatula and then dried in the vacuum oven at 80 °C for 8 h. The approximate area coated was 1cm X 1cm on each side. The electrodes were weighed after drying and the mass difference before and after coating was used to calculated the active material mass. The mass of the active material in each electrode was between 3mg and 5mg. Figure 2.5 shows the image of a typical slurry-coated macroelectrode.
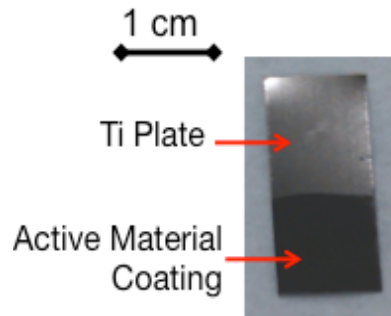
Figure 2.5 Image of slurry-coated macroelectrode (80% active material, 10% PVDF, 10% super P Li, solvent NMP) on a 0.127mm thick Ti foil, dried at 80 °C, under vacuum for 8h. Coated area= 1 cm X 1 cm on both sides. Mass of active material= 3mg- 5mg.

A scan rate of 2mVs^{-1} was used to perform CV experiments for capacitance measurement to avoid mass transfer limitations at fast scan rates. The experiments were performed at room temperature. The capacitance was estimated by integrating the area within the cyclic voltammogram (equation 2.2) [15].

$$\hat{C} = \frac{\int i \, dV}{s \cdot m \cdot \Delta V}$$
(2.2)

Here, $\hat{C}$ is the specific capacitance (Fg^{-1}), i is the current (A), ΔV is the potential window (V) within which the material was scanned, s is the scan rate (Vs^{-1}) and m is the mass of the active material mass (g) [15].

2.4   Results and Discussion

2.4.1 Physical Characterization:

Figure 2.6 shows the XRD patterns for the nitrides and carbides of Mo, V and W. These results confirm that the materials synthesized were phase pure and the conversion was complete. Typically metal oxides have diffraction peaks in the region between 10° to 30°. These peaks were absent in the XRD patterns measured for each of the materials. These results confirmed the structures of γ-Mo_2N, VN, VC and β-W_2N as *fcc* and β-W_2C and β-Mo_2C as orthorhombic (distorted *hcp*) structure.

The BET surface areas of the materials are listed in table 2.3. The surface areas were found to be similar to those reported previously [7-10].
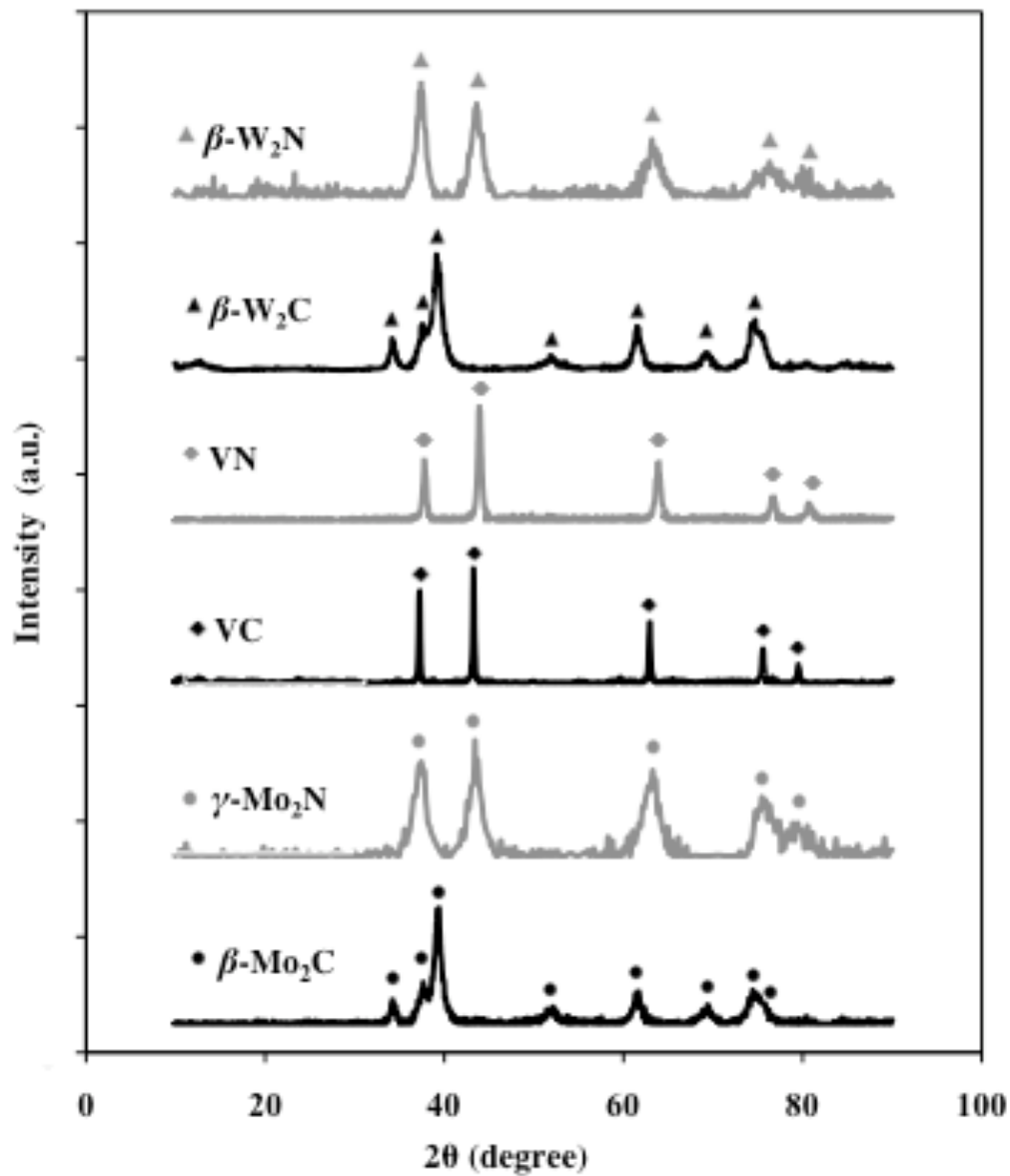
Figure 2.6 X-ray diffraction patterns of early transition-metal-nitrides and carbides after synthesis. Mo (circles), V (diamonds) and W (triangles) nitrides shown in gray. Mo (circles), V (diamonds) and W (triangles) carbides shown in black.

2.4.2 Electrochemical Characterization:

Figures 2.7-2.11 show cyclic voltammograms of early transition metal nitrides and carbides in aqueous electrolytes systems during voltage window expansion experiments performed to determine the stable operating voltage window. We took the stable operating voltage window for an electrode-electrolyte system to be the potential range within which the system generates repeatable cyclic voltammograms without decomposition of the electrolyte via, for example electrolysis. For aqueous systems, the maximum voltage window is typically limited to 1.23 V due to thermodynamic stability limits of water [14]. Table 2.3 provides a summary of the stable systems and the stable operating voltage window. Materials were described as unstable if there was evidence of loss of material due to, for example, corrosion.

Table 2.3 BET surface areas and electrochemical stability voltage window of early transition metal nitrides and carbides in aqueous 1M KOH and 0.5M H_2SO_4.

Material	Surface area m^2g^{-1}	Voltage Window 1M KOH V_{SHE}	Voltage Window 0.5M H_2SO_4 V_{SHE}
Mo_2N	152	Unstable	-0.2V to -0.6V
Mo_2C	55	Unstable	Unstable
VN	38	-1.1V to 0.1V	Unstable
VC	6	-0.8V to -0.1V	Unstable
W_2N	42	-0.7V to 0V	Unstable
W_2C	16	Unstable	-0.2V to -0.6V
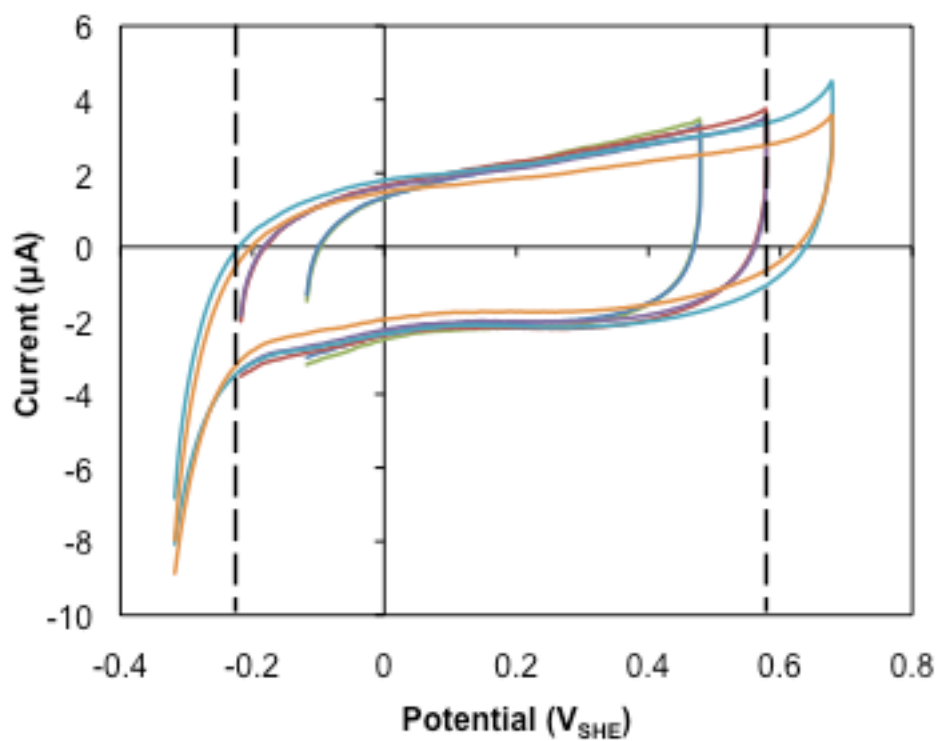
Figure 2.7 Cyclic voltammogram of Mo_2N in 0.5M H_2SO_4 at scan rate 50 mVs^{-1}, at room temperature. Showing 25th and 100th cycle within each voltage range. Stable operating voltage window indicated by dotted line, -0.2V to 0.6V *vs* SHE.
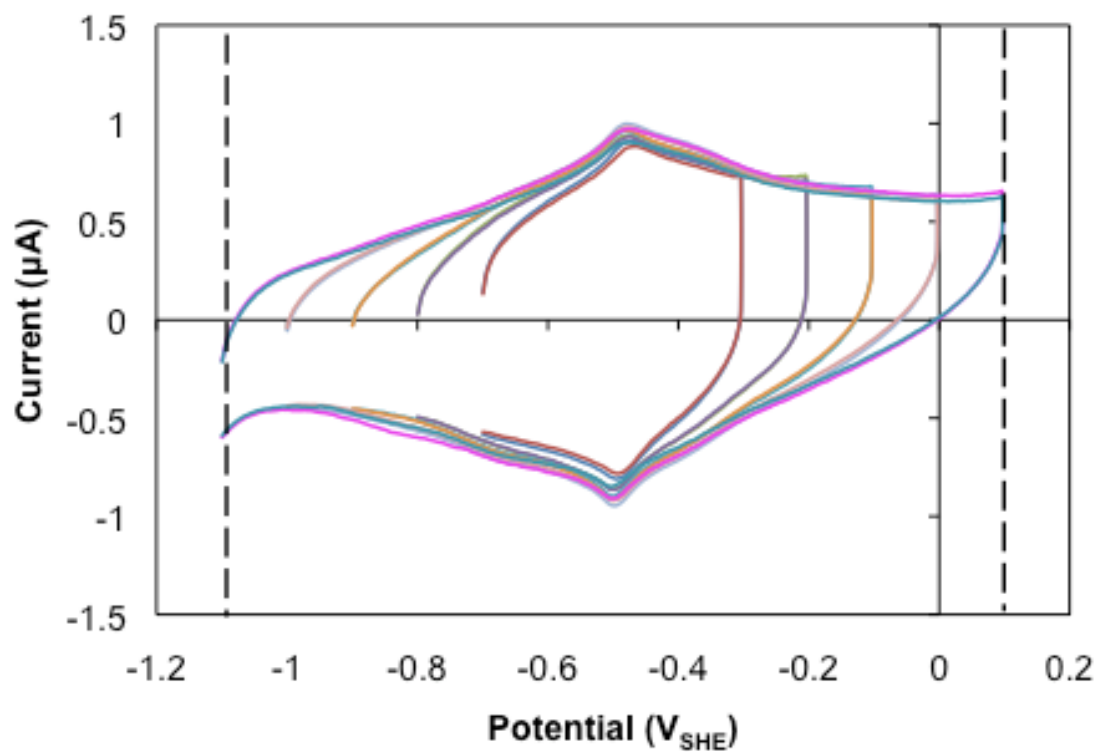
Figure 2.8 Cyclic voltammogram of VN in 1M KOH at scan rate 50 mVs^{-1} at room temperature. Showing 25th and 100th cycle within each voltage range. Stable operating voltage window indicated by dotted line, -1.1V to 0.1V *vs* SHE.
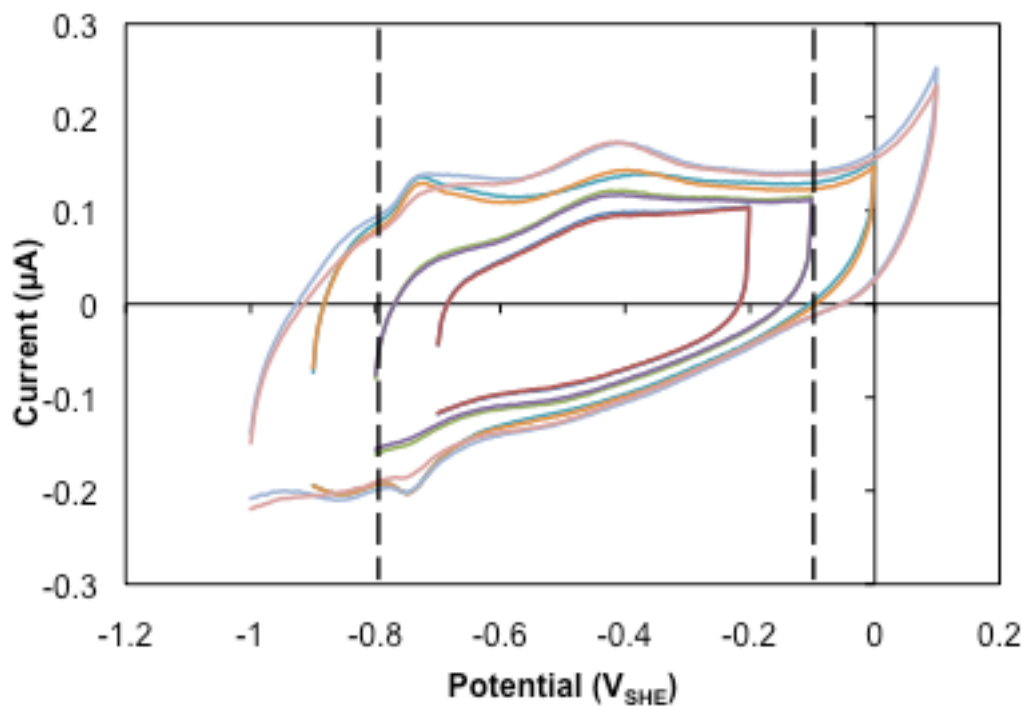
Figure 2.9 Cyclic voltammogram of VC in 1M KOH at scan rate 50 mVs^{-1} at room temperature. Showing 25th and 100th cycle within each voltage range. Stable operating voltage window indicated by dotted line, -0.8V to -0.1V *vs* SHE.
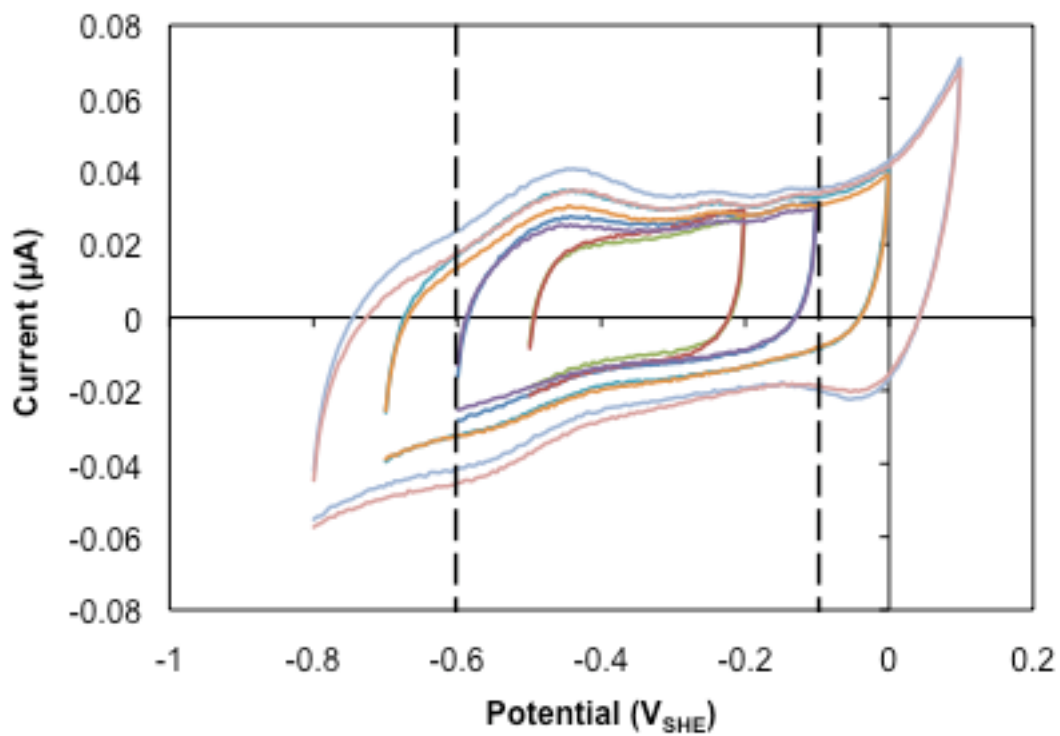
Figure 2.10 Cyclic voltammogram of W_2N in 1M KOH at scan rate 50 mVs^{-1} at room temperature. Showing 25th and 100th cycle within each voltage range. Stable operating voltage window indicated by dotted line, -0.7V to 0V *vs* SHE.
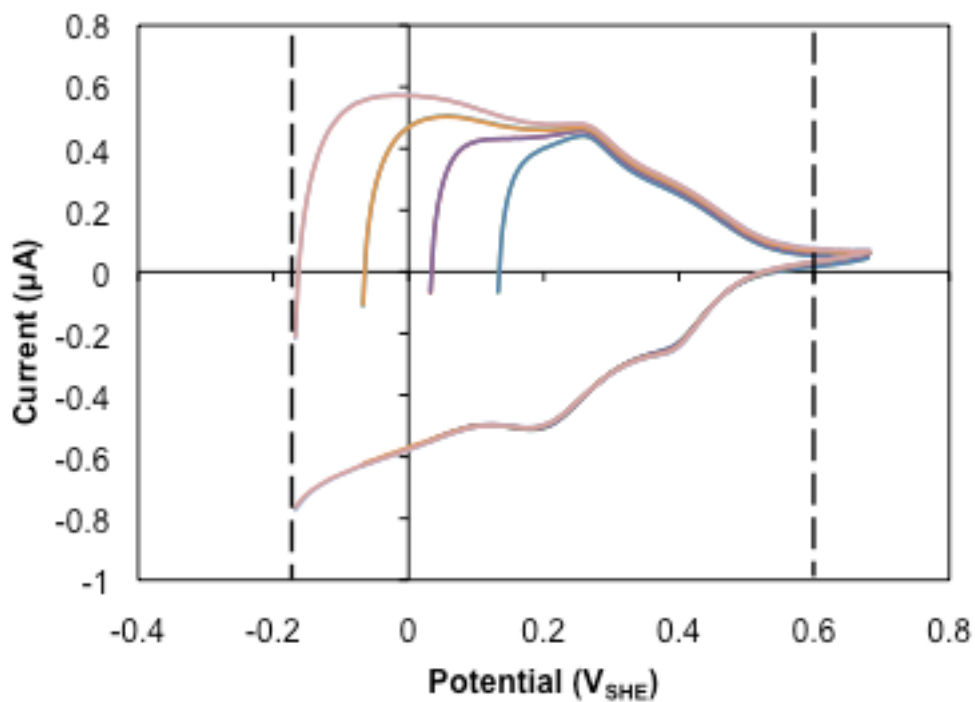
Figure 2.11 Cyclic voltammogram of W_2C in 0.5M H_2SO_4 at scan rate 50 mVs^{-1}, at room temperature. Showing 25th and 100th cycle within each voltage range. Stable operating voltage window indicated by dotted line, -0.2V to 0.6V *vs* SHE.

Table 2.4 provides a summary of measured gravimetric and areal capacitance for the 100th scan of the stable systems at a scan rate of 2mVs[-1]. The BET surface areas were used to calculate specific areal capacitances.

Table 2.4: Summary of gravimetric and specific areal capacitance of early transition metal nitrides and carbides in 0.1M aqueous H_2SO_4 and KOH within the stable operating voltage windows.

Material	Electrolyte	Voltage window V_{SHE}	Capacitance Fg^{-1}	Areal Capacitance μFcm^{-2}
Mo_2N	H_2SO_4	-0.2V to 0.6V	346	228
VN	KOH	-1.1V to 0V	210	552
VC	KOH	-0.8V to 0.1V	2.6	43
W_2N	KOH	-0.7V to 0V	25	60
W_2C	H_2SO_4	-0.2V to -0.6V	79	494

The results for the stability experiments on Au microelectrodes showed that VN, VC and W_2N were stable in KOH while W_2C and Mo_2N were stable in H_2SO_4. The β-Mo_2C material was not stable in either KOH or H_2SO_4 electrolytes. VN in KOH had the widest stable voltage window of 1.2V. Mo_2N in H_2SO_4 and W_2C in H_2SO_4 had stable operating windows of 0.8V, while W_2N and VC in KOH was stable over 0.7V. Except for Mo_2N in H_2SO_4, all the stable systems show redox peaks that are suggestive of pseudocapacitive charge storage. There was minimal peak separation was observed on the cyclic voltammograms of the

stable systems. These results suggest that the redox reaction were highly reversible within the stable operating voltage [14].

Although the cyclic voltammograms of Mo_2N in H_2SO_4 did not exhibit redox peaks, the possibility of pseudocapacitive charge storage could not be refuted. The cyclic voltammograms of Mo_2N in H_2SO_4 could suggest that there are several redox processes that overlap within the potential range, giving rise to constant current over the voltage window of 0.8V [15]. Similar observations have been made for MnO_2 in aqueous KCl or K_2SO_4, systems, that are known to store charge pseudocapacitively [16].

A better metric to evaluate pseudocapacitance contribution would be specific areal capacitance of the stable systems. Typically double layer capacitances for most materials are less than 50 μFcm^{-2} [15]. VN in KOH and W_2C in H_2SO_4 yielded highest capacitance of 552 μFcm^{-2} and 494μFcm^{-2}. These values were almost an order of magnitude higher than the expected double layer capacitance. Also, for Mo_2N in H_2SO_4 the areal capacitance of 228μFcm^{-2} was recorded, which exceeded the contribution from double-layer charge storage. Suggesting that for Mo_2N most of the charge storage is accomplished via pseudocapacitive mechanism.

Except for VC and W_2N in KOH, the specific areal capacitances for all of the nitrides and carbides were significantly higher than those expected for double-layer storage. In this study we used BET surface areas as an estimate for the electrode area active in charge storage. While BET surface areas are a good

estimate of the active area for charge storage, these values over-estimate the electrochemical area. The BET surface area estimates are based on N_2 physisorption on the surface of the materials, however, in case of electrochemical processes the adsorbates are solvated electrolyte ions, which are larger in size compared to N_2 atoms [15]. Thus, usage of BET surface areas in normalizing the capacitance provided more conservative values for areal capacitances as the actual electrochemical area active for charge storage could be smaller than the BET surface area.

The electrochemical surface areas of the electrode materials were not estimated in this work. The goal of the CV experiments was to screen materials and identify promising systems. Experimental procedures for estimating the individual contributions of the double layer charge storage compared pseudocapacitance have been discussed as future work in Chapter 5. The double layer capacitance values could be used to estimate the effective electrochemical surface area if the electrode materials, by using equation (1.3).

The results from CV suggested that pseudocapacitive mechanisms contributed to the overall capacitance. Although the areal capacitance of VC in KOH and W_2N in KOH were not significantly larger than the double layer capacitance expected for most materials, the redox peaks on their cyclic voltammograms (Figure 2.9-2.10) suggest that the pseudocapacitive mechanism contributes to charge storage. For both VC in KOH and W_2N in KOH, perhaps the

extent of pseudocapacitive charge storage mechanism is not as dominant as seen for VN in KOH, W_2C in H_2SO_4 and Mo_2N in H_2SO_4.

In terms of gravimetric capacitance, highest capacitance of 346 Fg^{-1} was reported for Mo_2N in H_2SO_4. This value is the highest reported capacitance for Mo_2N in H_2SO_4 [17]. Also, high gravimetric capacitance of 210 Fg^{-1} was reported for VN in KOH.

2.5 Summary:

Phase pure, nanostructured nitrides and carbides of V, Mo and W were synthesized and characterized in aqueous KOH and H_2SO_4 solutions. The stable operating-voltage windows of these materials were in the range of 0.7V- 1.2V. VN in KOH had the widest stability window of 1.2V. Based on cyclic voltammograms and capacitance values, pseudocapacitance contributes significantly to charge storage in Mo_2N, VN and W_2C. Although specific areal capacitances measured for VC and W_2N were not significantly larger than the double layer estimates, the redox peaks observed on their cyclic voltammograms suggest some contribution from pseudocapacitive charge storage.

Of the stable nitrides and carbides, VN in KOH (210 Fg^{-1}) and Mo_2N in H_2SO_4 (346 Fg^{-1}) demonstrated the highest gravimetric capacitances and widest stability windows. Their areal capacitances were nearly an order of magnitude higher than those expected based on double layer charge storage. Based on these results, VN in KOH and Mo_2N in H_2SO_4 were selected for a more detailed

investigation of their charge storage mechanisms and to establish the reactions involved in pseudocapactive charge storage.

2.6   References:

1. S.T. Oyama, The Chemistry of Transition-metal Carbides and Nitrides, Chapman and Hall Publisher, 1996.

2. S.T. Oyama, Catal. Today 15 (1992) 179.

3. J. G. Chen Chem. Rev. 1996, 96, 1477.

4. D. S. Pollock, Physical Properties of Materials for Engineers, Vol III, CRC Press, 1982.

5. M.R. Wixom, D.J. Tarnowski, J.M. Parker, J.Q. Lee, P.-L. Chen, I. Song, L.T.Thompson, Mat. Res. Soc. Symp. Proc. 496, Boston, 1-5 Dec., 1997, (1998) 643.

6. D. Choi, G.E. Blomgreen, P.N. Kumta, Adv. Mater. 18 (2006) 1178.

7. J.B. Claridge, A.P.E. York, A.J. Brungs, M.L.H. Green, Chem. Mater 12 (1) (2000) 132.

8. R. Kapoor, S.T. Oyama, J. Solid State Chem. 99 (1992) 303.

9. J.A. Schaidle, A.C. Lausche, L.T. Thompson, J. Catal. 272 (2010) 235.

10. L. Volpe, M. Boudart, J. Solid State Chem. 59 (1985) 332.

11. J. A Schaidle, Carbide and Nitride Based Catalyst for Synthesis Gas Conversion, Ph.D Thesis, University of Michigan, 2011.

12. B. D. Cullity, S.R. Stock, Elements of X-ray Diffraction, Vol 2, Addison Wesley Reading, MA, 1978.

13. T.-C Liu, W.G. Pell, B.E. Conway, J. Electrochem. Soc. 145 (6) (1998) 1882.

14. Bard, Allen. J.; Faulkner, Larry. R.; Electrochemical Methods 2nd Edition, John Wiley & Sons, inc., (2001).

15. B.E. Conway, Electrochemical Supercapacitors; Kluwer Academic/ Plenum Publishers, (1999).

16. P. Simon, Y. Gogotsi, Nature Materials, 7 (2008), 845-854.

17. P.Pande, P.G. Rasmussen, L.T. Thompson, J. Power Sources, 207 (2012) 212.

Chapter 3

Investigation of Charge Storage Mechanism

3.1 Introduction:

The focus of this chapter is to establish charge storage reactions for Mo_2N in H_2SO_4 and VN in KOH. The electrochemical performance characterization results described in chapter 2 suggested that these systems were the most promising among the early transition metal nitrides and carbides tested, due to their wide voltage windows and gravimetric capacitances. Additionally there have been reports for VN in KOH and Mo_2N in H_2SO_4 with capacitance in excess of 1300 Fg^{-1} and 300 Fg^{-1}, respectively [1,2]. Such large capacitances in excess of the purely double-layer-capacitance values have been attributed to pseudocapacitive charge-storage [1-3]. In order to improve and optimize performance of these systems, it is important to identify the species involved in charge storage and define the charge storage mechanisms.

To investigate an electrochemical charge-storage mechanism, the system can be divided into three key components: electrolyte ions, electrode material and the electrons transferred as a result of the electrode-electrolyte interaction. We characterized these components using various electrochemical and spectroscopic methods and charge-storage mechanisms for both VN in KOH and

Mo$_2$N in H$_2$SO$_4$ are proposed. In the following sections the experimental procedure and the results for role of each of these components is discussed.

3.2 Role of Electrolyte Ions:

To establish the role of electrolyte ions in the charge storage reactions we performed a series of ion isolation and substitution CV experiments. The K$^+$, OH$^-$, H$^+$ and SO$_4^{2-}$ ions were isolated by pairing them with inactive-counter ions. The counter ions CF$_3$SO$_3^-$ (triflate), (C$_2$H$_5$)$_4$N$^+$ (tetraethylammonium) and BF$_4^-$ (tetrafluoroborate) were selected as the counter ions as these are known to be redox inactive and do not dissociate in the voltage ranges of interest for the nitrides [3]. The K$^+$ and OH$^-$ ions were isolated as K(CF$_3$SO$_3$) and [(C$_2$H$_5$)$_4$N]OH, whereas the H$^+$ and SO$_4^{2-}$, were isolated as HBF$_4$ and [(C$_2$H$_5$)$_4$N]$_2$SO$_4$. Voltammograms were collected in aqueous solutions containing each of these salts.

The ionic strength of a solution I, is given by [4]:

$$I = \frac{1}{2}\sum_i z_i^2 c_i$$

(3.1)

where, z_i is the equivalent charge on the species i, and c_i is the molar concentration (M). The solution concentrations were adjusted to achieve constant ionic strengths of 0.1M for the solution containing K$^+$ (0.1M K(CF$_3$SO$_3$)) and 0.3M for the solution containing SO$_4^{2-}$ (0.1M [(C$_2$H$_5$)$_4$N]$_2$SO$_4$) . The solution pH was used to estimate the H$^+$ and OH$^-$ concentrations and ionic strengths. Additionally Mo$_2$N and VN were characterized in redox inactive salts of 0.3M [(C$_2$H$_5$)$_4$N]BF$_4$

and 0.1M $[(C_2H_5)_4N](CF_3SO_3)$, respectively, keeping the ionic strength consistent with the active electrolyte [3].

3.2.1 Materials and Methods:

The Mo_2N and VN were synthesized and the slurry-coated Ti foil macroelectrodes were prepared using procedures described in Chapter 2. Electrolyte solutions were prepared with ultrapure water (18.2 MΩ cm, Millipore Milli-Q Advantage A10). Mo_2N was tested in aqueous solutions of 0.1M H_2SO_4 (99.999%, Sigma Aldrich), 0.1M HBF_4 (Sigma Aldrich), 0.1M $[(C_2H_5)_4N]_2SO_4$ (Sigma Aldrich) and 0.1M and 0.3M $[(C_2H_5)_4N]BF_4$ (≥99%, Sigma Aldrich) to match the ionic strength of the active electrolyte. Hg|HgSO$_4$ (Sat. K_2SO_4, Radiometer Analytical) was used as the reference electrode for testing Mo_2N. VN was tested in aqueous solutions of 0.1M KOH (Alfa Aesar), 0.1M K(CF$_3$SO$_3$) (≥ 98%, Sigma Aldrich), 0.1M $[(C_2H_5)_4N]OH$(40% in H_2O, Sigma Aldrich) and 0.1M $[(C_2H_5)_4N](CF_3SO_3)$ (99%, Fluka). Hg|HgO (0.1M KOH, Radiometer Analytical) was used as the reference electrode for testing VN. A Pt flag was used as the counter electrode for both the Mo_2N and VN tests. Cyclic voltammetry (discussed in chapter 2) was performed in a three-electrode cell and each of these systems at a scan rate of 2mVs^{-1}. All of the experiments were performed in electrolyte solutions that were deaerated with N_2 for at least 30 minutes. A N_2 blanket was maintained during the experiments. The capacitance was calculated using equation 2.1.

3.2.2 Results and Discussion:

Voltammograms for Mo_2N and VN are shown in figures 3.1 and 3.2 respectively. The concentration of the electrolyte ions and their respective capacitances are listed in tables 3.1 and 3.2 for Mo_2N and VN respectively.
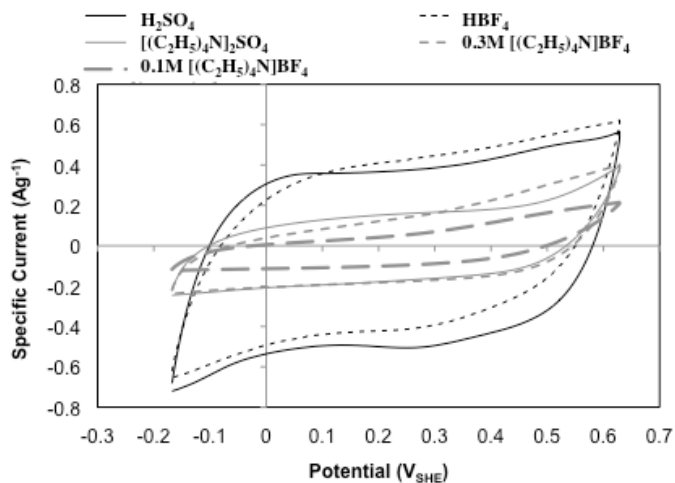
Figure 3.1 Cyclic voltammograms of Mo_2N in 0.1M H_2SO_4, HBF_4, $[(C_2H_5)_4N]_2SO_4$, $[(C_2H_5)_4N]BF_4$ aqueous solutions and 0.3M $[(C_2H_5)_4N]BF_4$ aqueous solution. Scan rate 2 mVs^{-1} at room temperature. N_2 blanket in the working electrode chamber.
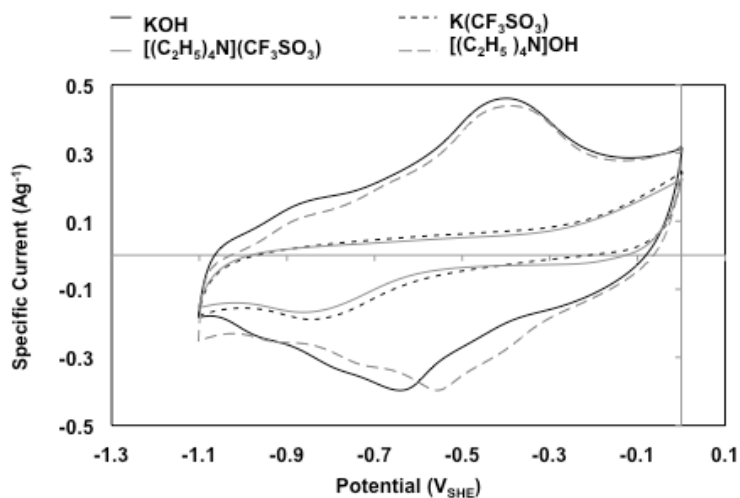
Figure 3.2 Cyclic voltammograms of VN in 0.1M KOH, $[(C_2H_5)_4N]OH$, $K(CF_3SO_3)$ and $[(C_2H_5)_4N](CF_3SO_3)$ aqueous solutions. Scan rate 2 mVs^{-1} at room temperature. N_2 blanket in the working electrode chamber.

Table 3.1 Summary of pH and ionic strengths of electrolytes solutions and gravimetric capacitances for Mo_2N at scan rate 2mVs^{-1}, at room temperature. H^+ and SO_4^{2-} were the active ions.

Electrolyte	pH	Ionic Strength (M)	Capacitance (Fg^{-1})
0.1M **H_2SO_4**	1.3	0.3	380
0.1M **H**BF$_4$	1.3	0.1	340
0.1M[(C$_2$H$_5$)$_4$N]$_2$**SO$_4$**	4.9	0.3	140
0.3M [(C$_2$H$_5$)$_4$N]BF$_4$	4.2	0.3	141
0.1M [(C$_2$H$_5$)$_4$N]BF$_4$	4.6	0.1	58

Table 3.2 Summary of pH and ionic strengths of electrolytes solutions and gravimetric capacitances for VN at scan rate 2mVs^{-1} at room temperature. K^+ and OH^- were the active ions.

Electrolyte	pH	Ionic Strength (M)	Capacitance (Fg^{-1})
0.1M **KOH**	12.9	0.1	234
0.1M **K**(CF$_3$SO$_3$)	9.3	0.1	65
0.1M[(C$_2$H$_5$)$_4$N]**OH**	12.8	0.1	228
0.1M [(C$_2$H$_5$)$_4$N]CF$_3$SO$_3$	8.1	0.1	61

From figure 3.1, the cyclic voltammograms for Mo_2N did not yield prominent peaks, however, the magnitudes of the capacitances (Table 3.1) implicated charge storage beyond that expected for formation of the electrochemical double layer. The capacitances for γ-Mo_2N in 0.1M H_2SO_4 (380 Fg^{-1}) and in 0.1M HBF$_4$ (340 Fg^{-1}) were similar, while those in 0.1M [(C$_2$H$_5$)$_4$N]$_2$SO$_4$ (140 Fg^{-1}) and 0.3M [(C$_2$H$_5$)$_4$N]BF$_4$ (141 Fg^{-1}) were lower. Note that the molarity for [(C$_2$H$_5$)$_4$N]BF$_4$ was adjusted to 0.3M to produce ionic strength of 0.3M similar to those for the other electrolytes. This result indicated that SO_4^{2-} and BF$_4^-$ had similar effects on capacitance and that for γ-Mo_2N in H_2SO_4, the H^+

was the most important active species for charge storage. To estimate the contribution of electrochemical double-layer capacitance for Mo_2N, cyclic voltammetry was carried out in a 0.1M $[(C_2H_5)_4N]BF_4$. This experiment yielded a capacitance of 58 Fg^{-1} which when normalized by the BET surface area gives 38 $\mu F\ cm^{-2}$, which is close to the expected double layer capacitance of 25-50 μFcm^{-2} [3].

The voltammograms (figure 3.2) and capacitances for VN in 0.1M KOH (234 Fg^{-1}) and 0.1M $[(C_2H_5)_4N]OH$ (228 Fg^{-1}) were similar, suggesting that OH^- was a key species in the charge-storage mechanism. Cyclic voltammograms for VN in 0.1M $K(CF_3SO_3)$ (65 Fg^{-1}) and 0.1M $[(C_2H_5)_4N](CF_3SO_3)$ (61 Fg^{-1}) were similar to each other, but capacitances were significantly lower from those in 0.1M KOH. Assuming that $CF_3SO_3^-$ was inactive, this result suggested that K^+ played a minor role in charge storage and may have been a spectator. The peak observed in the cyclic voltammogram for VN in $K(CF_3SO_3)$ and $[(C_2H_5)_4N](CF_3SO_3)$ at -0.85 V has been attributed to reactions involving minor contaminants in the electrolytes and/or $CF_3SO_3^-$. While this peak was reproducible, the absence of an oxidation peak suggests that the reduction of this species was an irreversible process.

3.2.3 Summary:

Results from the ion isolation experiments showed that OH^- and H^+ were the principal species participating in charge storage for VN in KOH and γ-Mo_2N in H_2SO_4, respectively, while K^+ and SO_4^{2-} were spectators.

3.3   Electrons Transferred:

In order to account for the electrons transferred during charge storage, the rest potential of the system was measured with varying concentrations of the electrolyte. The Nernst equation relates the equilibrium potential and active-species concentrations to the number of electrons participating in the charge transfer reaction [5].

$$E = E^o - 2.303\frac{RT}{nF}\log_{10}\left(\frac{a_{red}}{a_{ox}}\right) \tag{3.2}$$

Here, E is the measured potential difference across the cell (V), E^o the standard potential (V), R the universal gas constant (8.314 J mol^{-1}K^{-1}), T the temperature (K), n the number of electrons participating in the reaction, F is Faraday's constant (96485 Cmol^{-1}), and a_{red} and a_{ox} are the activities ($a_i = \gamma_i[i]$) of the reductant and oxidant, respectively. γ_i is the activity coefficient and $[i]$ is the concentration of species i. For Mo$_2$N in H$_2$SO$_4$, the measured pH was considered as the activity of the H$^+$, the active species for charge transfer. The pH of a solutions is defined as the single ion activity of H$^+$, given by equation (3.3) [5].

$$pH = -\log_{10}\gamma_{H^+}[H^+] \tag{3.3}$$

Similarly, in case of VN in KOH, pOH was used as the measure of the active species activity, given by equation (3.4) [5].

$$pOH = -\log_{10}\gamma_{OH^-}[OH^-] \tag{3.4}$$

The modified Nernst equations from used in our study thus give by equations (3.5) and (3.6) for the Mo_2N and VN are, respectively:

$$E = E^o + 2.303\frac{RT}{nF}pH \qquad (3.5)$$

$$E = E^o + 2.303\frac{RT}{nF}pOH \qquad (3.6)$$
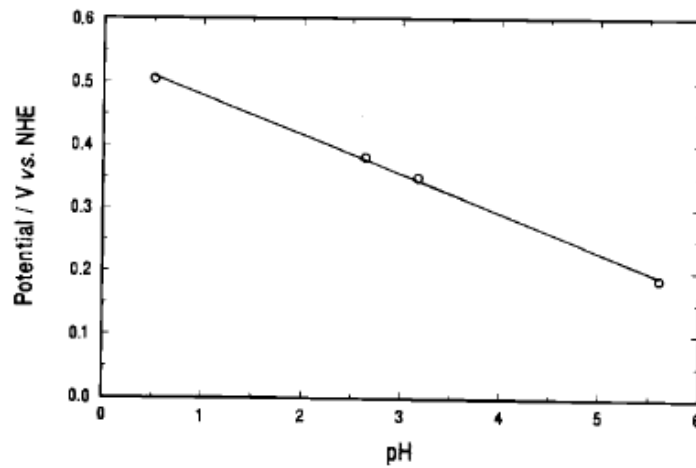
Figure 3.3 Dependence of Mo_xN film electrode rest potential with pH. Taken from [6].

In a similar rest potential versus pH measurement by Liu et al. for Mo_xN thin-film electrodes ($1\leq x \leq 2$) in varying concentrations of H_2SO_4, the rest potential (E_H) varied with pH and $\frac{\Delta E_H}{\Delta pH}$ had a relation of -60mV per pH [6]. Liu et al. synthesized their material by chemical vapor deposition of $MoCl_5$ in NH_3. [6]. Figure 3.3 is a reproduction of the rest-potential versus pH results from Liu et. al [6]. The pH dependence of the Mo_xN electrode was similar to the standard hydrogen electrode, which led them to propose that protons were active for

charge storage in Mo_xN and they proposed the reactions given by equations (1.7) and (1.8), involving a proton and an electron [6].

3.3.1 Materials and Methods:

The Mo_2N and VN were synthesized per the synthesis procedure discussed in chapter 2 and slurry-coated-Ti foil macroelectrodes were used for rest-potential measurements. These electrodes were prepared as per the procedure described in chapter 2. The experiments were performed in a three-electrode cell with a Pt-flag counter electrode. $Hg|HgSO_4$ (Sat. K_2SO_4, Radiometer Analytical) and $Hg|HgO$ (0.1M KOH, Radiometer Analytical) were used as the reference electrodes for testing Mo_2N and VN, respectively. All experiments were performed in electrolyte solutions deaerated for at least 30 minutes with N_2 prior to experiments. A N_2 blanket was maintained in the working electrode chamber during the experiment.

The Mo_2N was tested in H_2SO_4 aqueous solutions with concentrations varying from 0.0001M to 1M and VN was tested in KOH aqueous solutions with concentrations varying from 0.001M to 1M . Prior to the experiment the pH of the solution was measured using an Accumet BioBasic pH meter with an Ag/AgCl electrode. The pOH of the KOH electrolyte solutions was estimated by subtracting pH from 14 (14.0-pH). Chronopotentiometry experiments at zero current were performed. Here, voltage (V) was recorded as a function of time (t). The experiments were performed until $\frac{dV}{dt} \leq 10^{-5}$ Vs^{-1} to estimate the rest-potential.

3.3.2 Results and Discussion:

The measured pH and pOH values for the electrolytes tested are listed in table 3.3. Figures 3.4 and 3.5 show the chronopotentiometry results for Mo_2N and VN in varying electrolyte concentrations. The potential measured for the various systems was adjusted to the standard hydrogen electrode. The coefficient of the concentration term in the Nernst equation $2.303\frac{RT}{nF}$ is the slope of the plots 3.4(b) and 3.5 (b).

Table 3.3 Measured pH and pOH values of various electrolytes at room temperature, using a Accumet BioBasic pH-meter with Ag/AgCl electrode.

Concentration	H_2SO_4 pH	KOH pOH
1M	0.9	0.3
0.1M	1.4	1.3
0.01M	2.1	2.4
0.001M	3.2	3.5
0.0001M	4.1	-

The slope of the linear relationship for rest potential to pH for Mo_2N in H_2SO_4 aqueous solutions was -0.034±0.003, which corresponds to 1.7±0.2 electrons per H^+ reacted. The negative slope suggests that the electrons and the H^+ lie on the same side of the reaction. These results indicate that for every proton reacting with Mo_2N approximately 2 electrons being stored. These results obtained are not consistent with those observed by Liu et al. [6]. They performed the experiments with thin-film Mo_xN samples, synthesized by chemical vapor deposition. The influence of synthetic procedure on proton to electron stiochiometry has previously been observed for RuO_2 in aqueous H_2SO_4 [3]. The electrochemically grown RuO_2 films involve equal number of electrons and protons, while the thermally deposited films require a ratio of two electrons to a

proton [3,7]. The difference in the stoichiometry of protons to electrons for Mo_2N compared to results of Liu et al. could be attributed to the difference in the phase, crystallite size of the material and perhaps the difference in redox behavior of thick electrodes compared to thin-films [3]. The results from this study suggest the possibility of bulk material participation in charge storage in addition to the surface, which was not observed with thin-film electrodes by Liu et al.
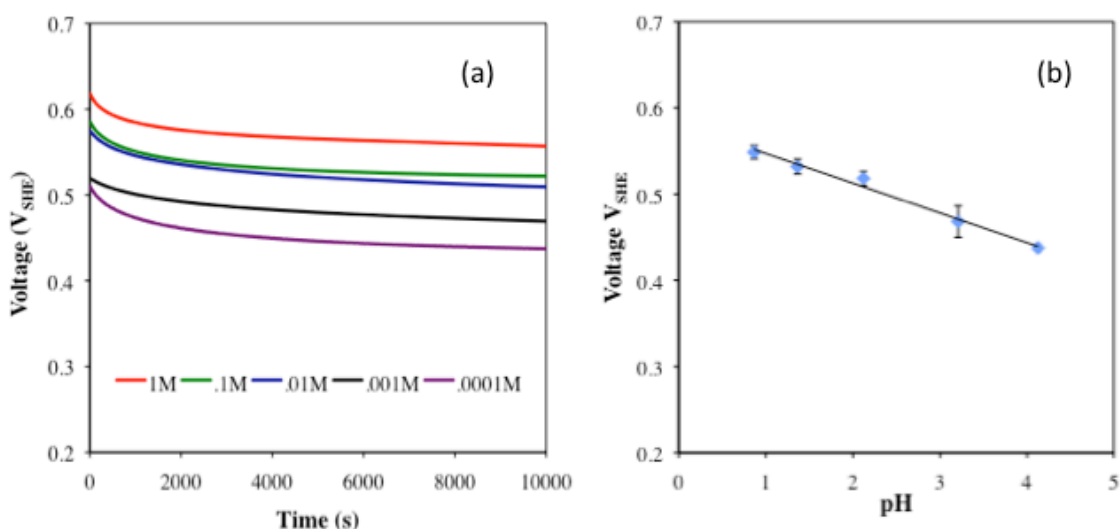
Figure 3.4 (a) Chronopotentiometry results at zero current for Mo_2N at varying concentrations of H_2SO_4 aqueous solutions, at room temperature. Experiments performed in a three-electrode cell, with N_2 blanket in the working electrode chamber (b) Measured rest-potential as function of pH for Mo_2N in H_2SO_4 aqueous solutions.

For VN, the slope of the potential to pOH dependence was 0.107±0.012, which corresponds to 0.58±0.09 electrons per OH⁻ reacted. As the slope for the VN rest-potential dependence to pOH is positive, electrons are released as OH⁻ react. Thus, for VN, approximately one electron is stored for 2OH⁻ that react.
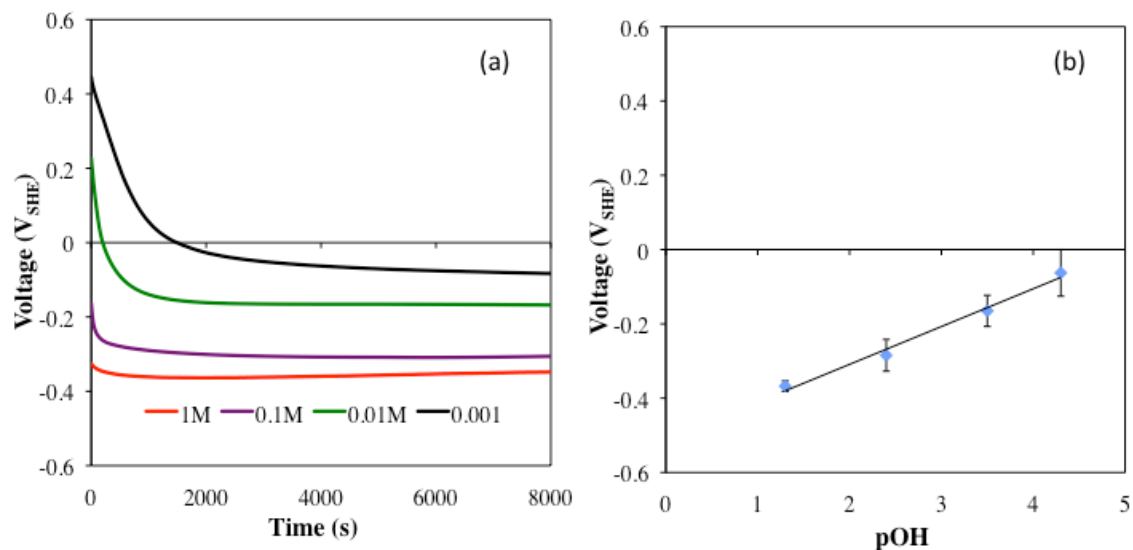
Figure 3.5 (a) Chronopotentiometry results at zero current for VN at varying concentrations of KOH, at room temperature. Experiments performed in a three-electrode cell, with N_2 blanket in the working electrode chamber (b) Measured rest-potential as function of pH for VN in KOH aqueous solutions.

3.3.3 Summary:

The results from the rest-potential experiments show that for every proton reacted with Mo_2N approximately two electrons are stored. While in VN for every electron stored there are approximately $2OH^-$ reacted.

3.4 *In situ* Characterization of the Changes in the Electrode Material:

In order to characterize the changes in the material during charge storage, we applied spectroscopic techniques in conjunction with electrochemical measurements. *In situ* x-ray absorption spectroscopy (XAS) allows monitoring of the detailed local atomic co-ordination and chemical/oxidation state of a specific element of interest [8].

In XAS, the x-ray energy is scanned through binding energy of the core shell of an element, which leads to a substantial increase in the absorption, giving rise to an absorption edge. The energy at which the x-rays are absorbed by an atom is element specific and is called the edge energy [8]. Core shells (K, L or M shell) for an element have discrete binding/edge energies giving rise to K, L or M x-ray absorption edges [8]. The XAS spectra are typically divided in to two regions: (i) X-ray absorption near-edge spectra (XANES) and (ii) Extended X-ray absorption fine structure (EXAFS). The XANES region is about 20 eV above and below the absorption edge, while the EXAFS region can extend as much as 1000 eV beyond the absorption edge [8].

XAS can be carried out in transmission and/or fluorescence mode. In transmission mode, ionization chambers are placed in front of and behind the sample. Incident and the transmitted x-ray flux are measured to account for the absorption. In fluorescence mode, the absorption of x-ray results in photoelectron emission, which leaves the atom in an excited state. Fluorescent x-rays are emitted to repopulate the core-hole. The fluorescent x-rays interact, proportional to the x-ray absorption coefficient of the material [8].

3.4.1 Materials and Methods:

For the characterization of Mo_2N and VN, spectra at the Mo K-edge (20000 eV) and V K-edge (5465 eV) were collected. XAS measurements were performed in transmission mode at the bending magnet beam line station D of the DND-CAT (Sector 5), at the Advanced Photon Source (APS). A water cooled Si(111) double crystal monochromator was used for energy selection and

incident and transmitted x-ray intensities were measured using Ar filled ion chambers at 1 atm pressure with an applied voltage of 300 V. The beam size was defined as 1mm x 3 mm using slits and the incident photon flux was ~10^{10} photons/s.
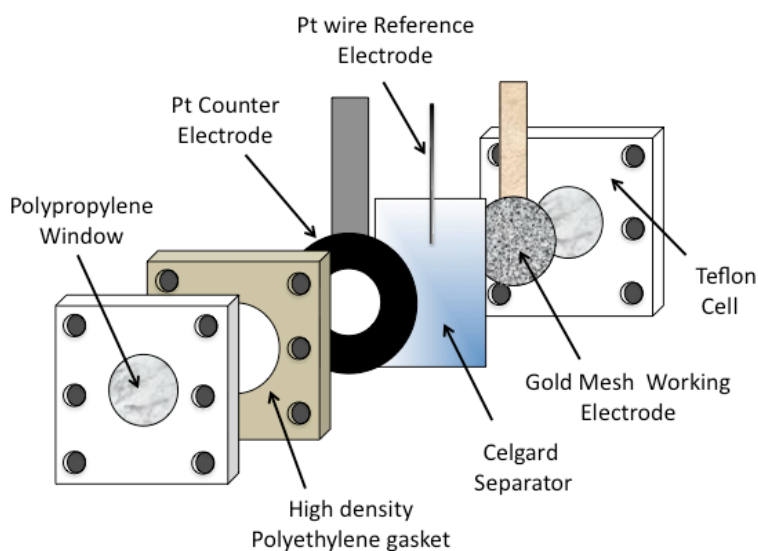
Figure 3.6: Schematic of the in-situ XAS cell. Cell Dimensions 5cm X 5 cm. Polypropylene window 1.5 cm in diameter. Assembled cell thickness ~0.8 cm.

In situ XAS measurements were performed using the cell shown in figure 3.6. For Mo_2N the working electrode was prepared by packing a gold plated tungsten gauze (50 mesh, Alfa Aesar) with a slurry of 70% Mo_2N, 20% carbon black (Super P Li), 10% polyvinylidene fluoride (Kynar, Arkema) in N-methyl-2-pyrrolidone (99.95%, Alfa Aesar) solvent. The electrodes were dried in vacuum for 8h at 80 °C and then calendered to a thickness of ~100 µm. The size of the electrode was 5/8 inch in diameter.   Pt black (Alfa Aesar) coated Ti foil (99.7%, Aldrich) was used as the CE and a Pt wire (99.95%, Alfa Aesar, 0.5 mm thick) was used as a quasi-reference electrode. The measurements were performed in

aqueous 0.1M H_2SO_4 aqueous solution. Celgard 3501 was used as the separator.

For VN characterization, the working electrode were prepared by coating carbon paper (Toray Carbon Paper TGP-H-060, 190 μm) with a of 70% VN, 20% carbon black (Super P Li), 10% polyvinylidene fluoride (Kynar, Arkema) in N-methyl-2-pyrrolidone (99.95%, Alfa Aesar) solvent. A doctor blade system was used to prepare the coating with a thickness of 5 μm. A high surface area activated carbon fabric (Kynol, ACC-507-15, 1300 m^2g^{-1}) was used as the counter electrode. A Glass fiber separator (El-Cell, 0.65 mm thickness) and a Pt wire (99.95%, Alfa Aesar, 0.5 mm thick) quasi-reference electrode were used. In order to minimize x-ray absorption from the electrolyte ions, LiOH was used as the active electrolyte instead of KOH. K has x-ray absorption energy of 3608.4 eV, while Li has x-ray absorption energy of 54eV. VN was tested in 0.1M LiOH aqueous electrolyte solution.

In addition to Mo_2N and VN, model compounds were tested to establish the relation between the edge shift and oxidation state. Mo foil and Mo(IV) oxides (99%, Strem Chemicals) were used as standards for Mo. V foil, V(II) oxide (99% Alfa Aesar), V (III) oxide (98%, Sigma Aldrich), V(IV) oxide (Strem Chemical), V(V) oxide (99.5% Sigma Aldrich) were used as standards for V.

Prior to adding the electrolyte solution, XAS measurements were made on the "as-is" sample. The deaerated electrolyte solution was then added and the cell was sealed. CV measurements were performed using a CH-instruments CH-

660D potentiostat and the stable operating-voltage range was determined *vs* a Pt-wire reference electrode. The voltage window was divided in to discrete potential steps as shown in figures 3.7 and 3.8 for Mo_2N and VN respectively, and *in situ* XAS measurements were performed at these potentials. The XAS spectra were collected once while increasing the voltage and then second time while decreasing the voltage, thus completing a cycle. Each potential was applied and the current was allowed to equilibrate for at least 1000 s at each voltage prior to making the XAS measurements.

For Mo_2N, three scans were collected from 19800 eV to 20980 eV at each applied voltage for better data resolution and averaging. The data were analyzed using ATHENA software [9]. The energy was calibrated with reference to a Mo foil internal reference with the first inflection point of Mo foil defined at 20000 eV . As per the standard procedure, a linear pre-edge line (200 eV to 50 eV before edge) was subtracted from the spectra for the XANES region and a cubic spline used to remove the EXAFS background [9]. The radial structure functions were obtained by Fourier transformation of $k^3 \chi(k)$ using a k range of 1.5–15 $Å^{-1}$ [9].

For VN, two scans were collected from 5365 eV to 6108 eV at each applied voltage for better data resolution and averaging. Only the XANES region was analyzed. ATHENA software was used for analysis. An energy shift based on the V foil (5465 eV) was applied to account for instrumentation error. A linear pre-edge line (200 eV to 50 eV before edge) was subtracted from the spectra for the XANES region.

3.4.2 Results and Discussion

Figures 3.7 and 3.8 are the cyclic voltammogram for Mo_2N in H_2SO_4 and VN in LiOH, measured in the *in situ* XAS cell. The voltage window (0.8V for Mo_2N and 1.1V for VN) and the shape of the cyclic voltammograms observed for both materials in the in-situ cell were similar to the ones in the three-electrode cell (figures 3.1 and 3.2), in terms of their operating-voltage windows and redox behavior. These results suggested that the electrochemical performance observed in the *in situ* cell was similar to that observed with the three-electrode system.
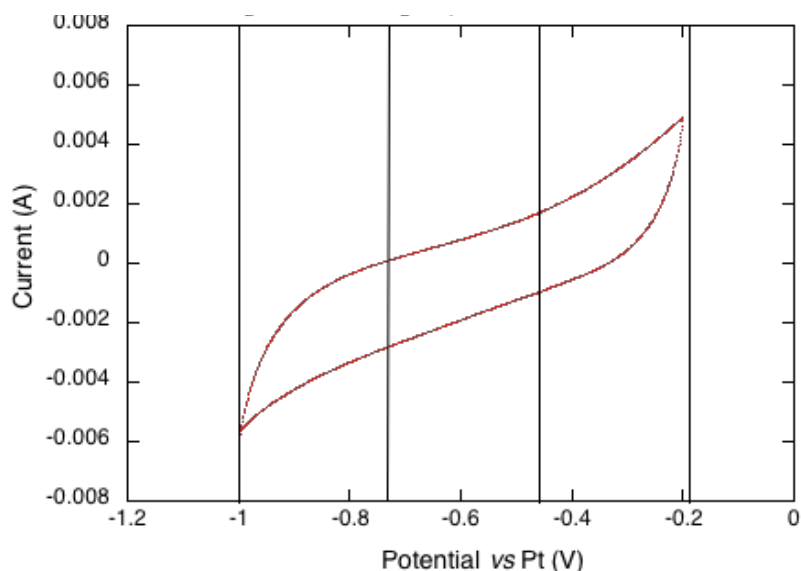
Figure 3.7 Cyclic voltammogram of Mo_2N in 0.1M H_2SO_4 in the XAS cell vs Pt reference electrode, at scan rate of $10mVs^{-1}$, at room temperature. The verticals lines indicate the discrete potentials at which the XAS spectra were collected.
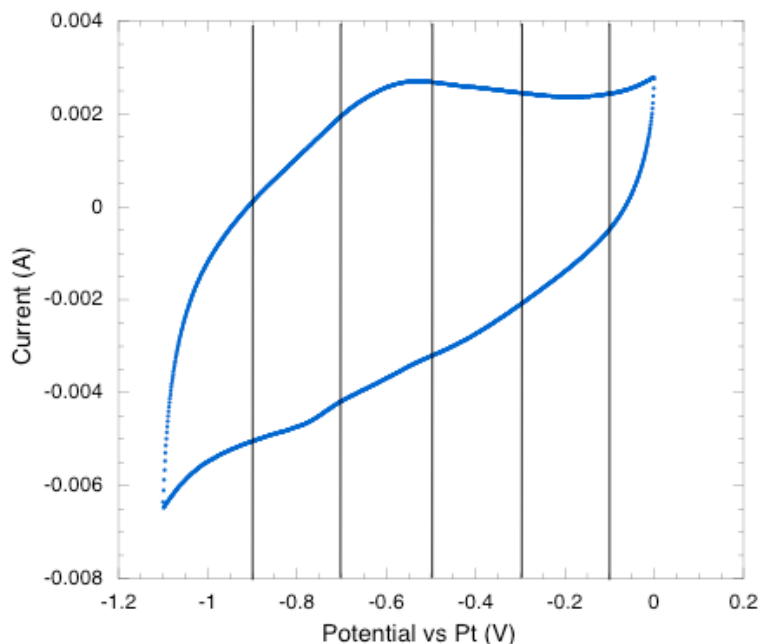
Figure 3.8 Cyclic voltammogram of VN in 0.1M LiOH in the XAS cell vs Pt reference electrode, at scan rate of 50 mVs^{-1}, at room temperature. The verticals lines indicate the discrete potentials at which the XAS spectra were collected.

The XANES spectra for Mo_2N and MoO_2 are shown in figure 3.9. All of the spectra are similar in both shape and energy, with a weak, poorly resolved shoulder on the rising edge and an edge maximum at ~20020 eV [11]. On addition of electrolyte the Mo_2N edge becomes slightly broader than in the "as-is" spectrum, but does not show any dramatic change suggesting that the overall Mo environment is largely unchanged. The edge energy can be defined as the first inflection point, taken as the maximum in the first derivative. Figure 3.10 shows the shift in the edge energy, when the potential is applied between -0.73V to -0.19V vs Pt wire quasi-reference electrode. This shift was completely reproducible as the forward and reverse scans overlapped. This suggested that Mo was oxidized as the potential was increased.
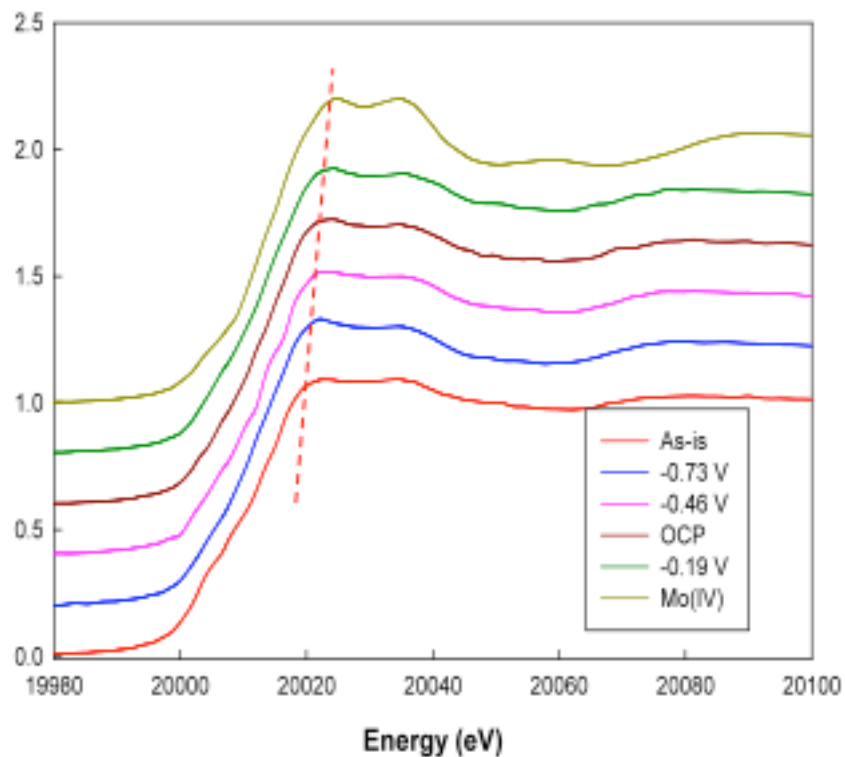
Figure 3.9 Normalized XANES spectra for MoO_2 and Mo_2N 'as-is' and Mo_2N in 0.1M H_2SO_4 at different potentials. Red dotted line shows the shift in the edge energies.
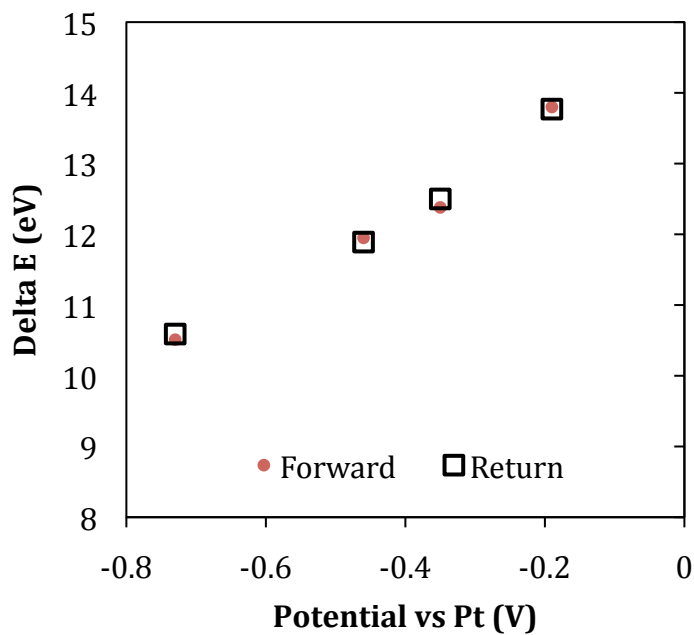
Figure 3.10 Edge shift for the Mo –K edge compared to Mo foil, at the increasing (forward) and decreasing (return) applied voltages *vs* Pt wire.

For Mo_2N, at each potential when it is increased from -0.73V to -0.19V *vs* Pt wire and back, an edge shift of ~ 3.3 eV (figure 3.10) was observed. A 3.75 eV per oxidation state shift in edge energy for the model compounds Mo(0) and Mo (IV) was observed. Using the eV per oxidation state shift relationship for the model compounds, we estimated removal of ~1 electron per Mo from a band of predominately Mo character as the voltage is increased.
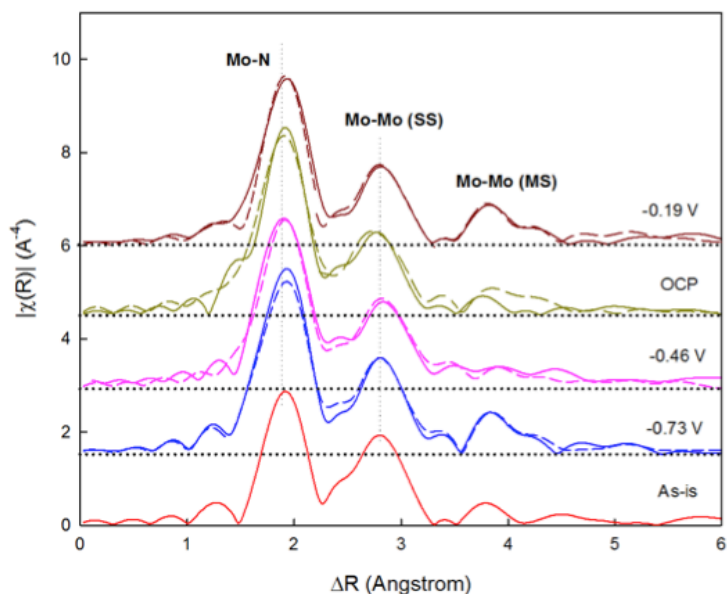
Figure 3.11 Fourier transforms of the k^3-weighted EXAFS data for Mo2N "as- is" and at applied potentials. Solid line represents data during increasing potential (forward) ; Dashed line represents Data measured while decreasing potential (reverse).

The Fourier transforms of the extended x-ray absorption fine structure (EXAFS) data for Mo_2N are shown in figure 3.11. These spectra are similar to those in previous reports [11]. The spectra collected for the "as-is" sample, and those collect at various potentials resembled each other. The Fourier transforms are dominated by peaks at ~2 Å and ~2.8 Å, which were attributed to Mo-N

nearest neighbors and Mo-Mo next-nearest neighbors, respectively [11]. The similarity of these spectra suggested that the local structure around Mo remained unchanged when electrolyte was added and when potential was applied in the forward and reverse directions. However, small but highly reproducible changes in the outer-shell scattering were observed around ~3.8 Å. This peak was attributed to Mo-N-Mo multiple scattering [11]. The intensity of this peak increased significantly at the extreme potentials (-0.73 V and -0.19 V). This suggested that the structure was more ordered at these extremes than at the intermediate potentials. This change in the Mo-N-Mo multiple scattering peak reflected some reproducible structural change/distortion.

○ Mo ● N
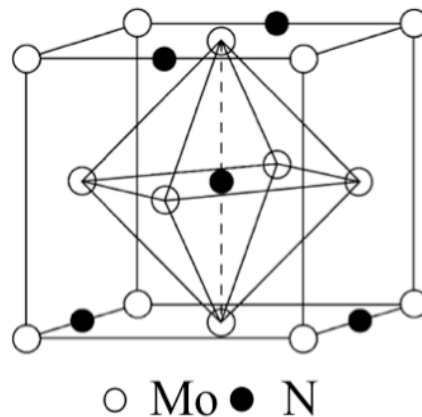
Figure 3.12 Structure of Mo_2N.

To understand the changes in the multiple scattering peak, we examined the crystal structure of Mo_2N (figure 3.12). Mo_2N has an *fcc* structure with N partially occupying the octahedral sites, while its tetrahedral sites are vacant. In the Mo_2N lattice there is one octahedral site per Mo, and two tetrahedral sites per Mo [10]. The Mo_2N EXAFS data suggested that key aspects of the structure did not change and change in the multiple scattering peak did not affect the Mo-N or

Mo-Mo distances. Given that Mo_2N interacts with H^+ during charge-storage in acidic media, one possibility for the change in the multiple scattering peak could be H incorporation into the vacant octahedral and/or tetrahedral interstitial sites.

Transition metals are known to form interstitial solid solutions/alloys with H. These interstitial solid solutions/alloys are governed by empirical rules developed by Hägg [12]. The Hägg rule proposes that if the ratio of non-metal atomic radii to the parent metal atomic radii is between 0.59 and 0.41, the non-metal will occupy the octahedral positions. However, if the ratio of the atomic radii of the non-metal to the parent-metal is between 0.41 and 0.23, the non-metal would preferentially occupy the tetrahedral sites[12].

The crystal structure of Mo_2N is more like Pd than Mo. This similarity in Mo_2N and Pd crystal structures has been attributed to the similarity in their *s-p-d* band structure by the Engel-Brewer theory [10]. Incorporation of H into the metal lattice has been studied for PdH_x ($0 \leq x \leq 2$). Here H atoms occupy the interstitial sites of the *fcc* Pd cell. The ratio of H (53 pm) to Pd (163 pm) atomic radii is 0.32 [12]. Based on this ratio the Hägg rule predicts occupation of the Pd tetrahedral sites by H [12].

In another study by Caputo et al., reported results from *ab intio* simulations in which sub-stoichiometric amounts of H were added to the Pd lattice (PdH_x) ($0 \leq x \leq 1$) [13]. They proposed that both the occupation of octahedral and tetrahedral sites would lead to the expansion of Pd lattice parameter (a). The Pd lattice expanded from a= 3.97Å to 4.02Å in case of

octahedral occupation and 4.05Å for tetrahedral sites occupation when one H

atom was added to Pd [13]. Also, the enthalpy of formation for the tetrahedral

site occupation was lower than those estimated for octahedral site occupation.

The results by Caputo et. al suggested that occupation of tetrahedral interstitial

site by H is energetically more favorable. This phenomenon leads to increase in

Pd-Pd bond distance and distorts the long-range order of the crystal [13]. These

results are in line with Hägg rule predictions of tetrahedral sites occupation by H

in Pd. For the Mo-H interaction, the ratio of H (53 pm) to Mo (139 pm) atomic

radii is 0.38 [12]. Based on the Hägg rule we speculate that Mo tetrahedral sites

would be occupied by H. Figure 3.13 (b) shows a schematic for H incorporated

in the tetrahedral sites of Mo_2N. As H is incorporated in the tetrahedral site of the

Mo_2N structure, it could distort the Mo-Mo long-range order in the crystal as seen

in Pd [13], This distortion could lead to the change in the Mo-Mo multiple

scattering peak at ~3.8 Å, however the Mo-N and Mo-Mo interaction would not be

affected.
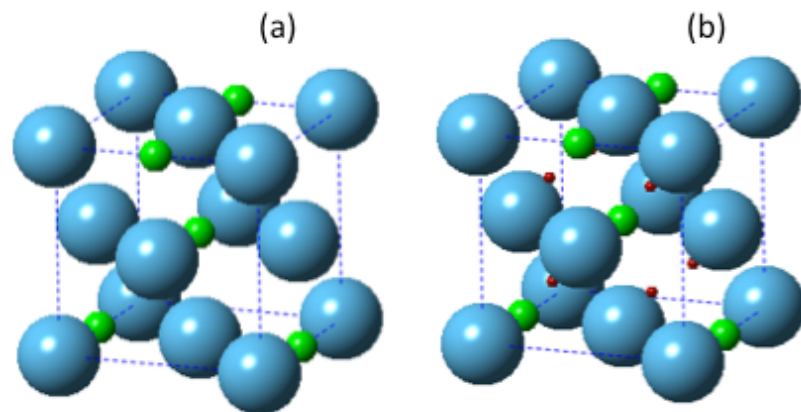
Figure 3.13 CrystalMaker Models for (a) Mo_2N and (b) H incorporated in the tetrahedral interstitial sites of Mo_2N. Blue spheres represent Mo, green spheres represent N and red spheres represent H.

In terms of the availability of the tetrahedral sites, up to two H can be incorporated per Mo or four H in Mo_2N.

For VN, the XANES spectra at different voltages between -0.9V and -0.1V *vs* Pt wire are shown in figure 3.14. Except for the "as-is" sample all the spectra shows a similar pre-edge feature around 5470 eV which shows that the local geometry does not change and the edge around 5488 eV for spectra collected at -0.9V to -0.1V vs Pt wire. There were no dramatic changes in the shape of the spectra, however, it was observed that the pre-edge and edge energy increase slightly as the potential is increased from -0.9V to -0.1V vs Pt wire. Compared to the spectra for the "as-is" sample the addition of electrolyte causes a shift in the edge and the pre-edge energy, but the overall shape of the spectra remained the same. Figure 3.15 shows the shift in the edge energy when the potential was applied between -0.9V to -0.1V vs Pt wire. This shift was reproducible for the forward and reverse scans.
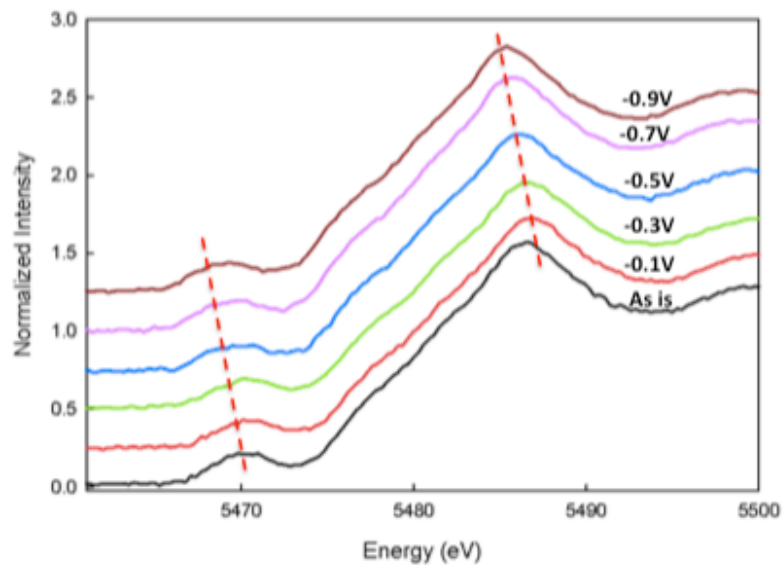
Figure 3.14 Normalized XANES spectra for VN 'as-is' and VN in 0.1M LiOH at different potentials vs Pt wire, at room temperature. The dotted red lines indicate the pre- edge (~5470 eV) and edge (~5488 eV) features.
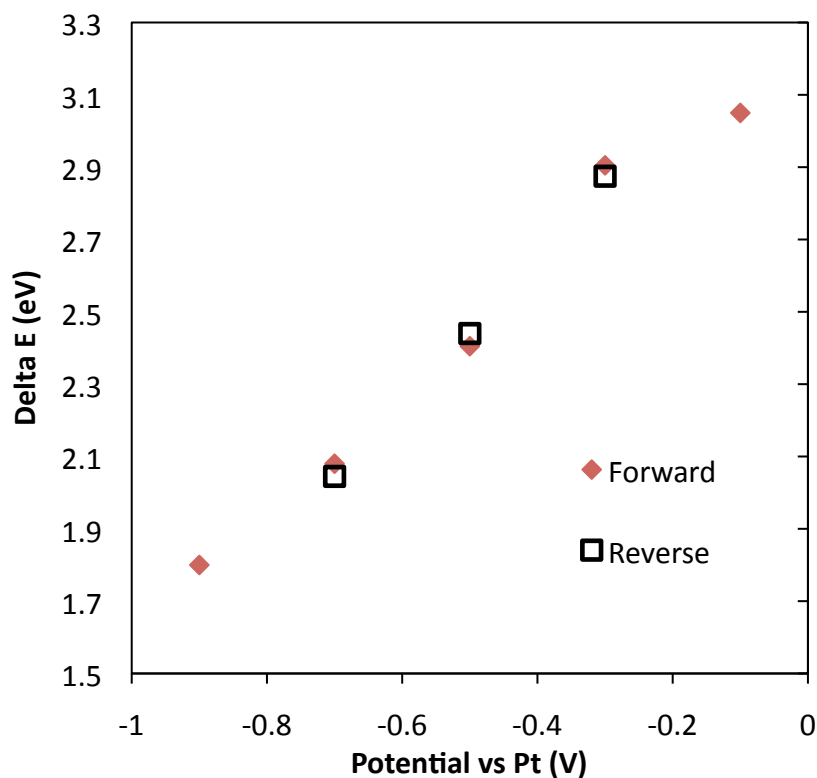
Figure 3.15 Edge shift for the V –K edge compared to V-foil for increasing (forward) and decreasing (reverse) applied voltage *vs* Pt wire.

From figure 3.15, a 1.2 eV edge shift was observed for VN with in applied the voltage range (-0.9V to -0.1V *vs* Pt wire). A ~0.95 eV per oxidation state shift in edge energy was recorded for the model compounds V(0), V(II), V(III), V(IV) and V(V). This relationship (~0.95 eV per oxidation state shift) was used to estimate the change in oxidation state of VN. These data corresponds to removal on average of ~1 electrons per V as the voltage is increased from -0.9V to -0.1V.

3.4.3 Summary

In situ characterization of Mo_2N in H_2SO_4 XAS was performed. Analysis of the XANES spectra for Mo suggested that ~1 electron was removed or added per Mo during material cycling with in its voltage window of -0.73V to -0.19V vs Pt wire. The EXAFS results show that although the local structure of Mo did not change with regards to the Mo-N and Mo-Mo distances, there were reversible changes in the Mo-N-Mo multiple scattering peak with voltage. These changes have been attributed to H incorporation into the interstitial sites. According to the Hägg rule, H would prefer the vacant tetrahedral sites compared to partially-occupied octahedral sites. The tetrahedral sites could accommodate up to four H in Mo_2N. As XAS experiments were performed in transmission mode these results provide an average picture of the changes in the material during charge storage. To account for surface contribution to charge storage thin-film electrodes will have to be tested. Further details about experiments designed to isolate surface contribution have been discussed in chapter 5.

For VN in LiOH, analysis of the XANES spectra suggested that there was ~1 electron being removed and added per V during material cycling within its

voltage window. Further analysis of the EXAFS region is needed to understand the changes in the V ligation during cycling.

3.5 Conclusions

The Mo_2N in H_2SO_4 and VN in KOH systems were characterized by various techniques in order to establish its charge storage mechanism. The results discussed in this chapter identify the role of the electrode and electrolyte species involved in electrochemical charge storage in Mo_2N in H_2SO_4 and VN in KOH.

3.5.1 Charge storage reaction of Mo_2N in H_2SO_4

The H^+ was found to be the active electrolyte ion by characterizing Mo_2N with cyclic voltammetry in a series of electrolytes solutions selected by pairing H^+ and SO_4^{2-} to inactive counter ions. Rest potential dependence of Mo_2N to pH of the solution was determined. The slope of this linear relationship was used to estimate the number electrons transferred per proton reacted with Mo_2N based on the Nernst equation. The results for this study indicated that for every proton H^+ reacted with Mo_2N approximately two electrons were stored.

In situ XAS results were used to determine changes in Mo_2N during charge storage. The analysis of the XANES suggested that as the voltage is increased there is ~ 1 electron was removed per Mo removed, hence for Mo_2N we would expect a 2 unit change in the oxidation state during charge storage. The analysis of EXAFS region shows that there was no change in the immediate local structure of Mo as the potential was increased and then reversed. However, a reversible change in the Mo-N-Mo multiple scattering peak was

observed. Based on the Hägg rule and literature on H insertion in Pd (*fcc*), it is proposed that H is incorporated in the tetrahedral sites of the *fcc* Mo_2N lattice, leading to distortions. This could lead to the change in Mo-N-Mo multiple scattering peak with potential depending upon the extent of H incorporated. As there are 2 tetrahedral sites per Mo, Mo_2N can accommodate up to 4 hydrogen atoms.

The combining the results from sections 3.2 to 3.4 we propose the following reaction (3.7) for Mo_2N charge storage in acidic media:

$$Mo^{\delta}_2N + 2H^+ + 4e^- \leftrightarrow Mo^{\delta-1}_2N(H_{abs})_2 \tag{3.7}$$

It is proposed that the protons interacting with Mo_2N would occupy interstitial sites as absorbed hydrogen during charging and are released during discharge. The XAS results suggest that hydrogen incorporation into the Mo_2N is accompanied by reduction of Mo. As the XAS experiments were performed in transmission mode, the extent of surface or bulk material participation for hydrogen adsorption could not be distinguished. There is possibility of differing extent of surface versus bulk reduction of Mo_2N during charge storage. The XAS experiments probed the average oxidation state change, during charge storage.

$$Mo^{\delta}_2N + 2H^+ + 4e^- \leftrightarrow Mo^{\delta-1}_2N + H_2 \tag{3.8}$$
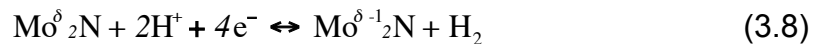
The possibility of hydrogen evolution reaction given by equation (3.8) is discounted due to the operating voltage window of Mo_2N in H_2SO_4. The electrochemical stability of Mo_2N in aqueous H_2SO_4 system yields 200mV overpotential to the hydrogen evolution reaction as shown by CV results in

chapter 2. Based on equation (3.7) the theoretical capacitance for Mo_2N (206 $gmol^{-1}$) is estimated as 2340 Fg^{-1} using Faraday's constant (96485 C mol^{-1} per electron) with in a 0.8V voltage window.

3.5.2 Charge storage reaction of VN in KOH

The hydroxyl ion was found to be the active species involved in charge storage reaction by characterizing VN with cyclic voltammetry in a series of electrolyte solutions selected by pairing K^+ and OH^- to inactive counter ions. The rest potential dependence on OH^- activity was established. The slope of this linear relationship was used to estimate the number of electrons transferred per OH^- reacting with VN. As the slope was positive, OH^- and the electron are on the opposite sides of the reaction.

In situ XAS characterization was used to determine the change in VN during charge storage. LiOH was used as a substitute for KOH as Li has less absorbance compared to K. Only the XANES region of the XAS spectra were analyzed. These results suggested that there is ~1 electron change in the V valence during charge storage.

Based on these findings we propose the following reactions for charge storage in VN in basic media:

$$2OH^- \leftrightarrow H_2O_2 + 2e^- \tag{3.9}$$

$$V^\delta N + 2OH^- \leftrightarrow V^{\delta-1}N + H_2O_2 + e^- \tag{3.10}$$
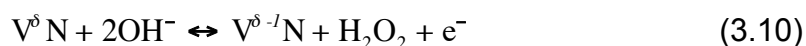
The charge storage mechanism of VN in KOH involves reduction of VN during charging. It is proposed that VN provides sites for combination of the 2OH$^-$ to form H_2O_2 in solution given by equation (3.9). This reaction results in reduction of V and storage of an electron as shown by equation (3.10). As the pre-edge feature did not show a significant change it is suggested that perhaps the local geometry of VN does not change significantly during charge storage. Further analysis of the change in the local structure by EXAFS is necessary to better understand the charge storage mechanism and the possibility of ligand substitution.

As the XAS experiments were performed in the transmission mode, the specific changes in the oxidation states of the surface or bulk material could not be identified. There could be different extent of redox participation of VN surfaces compared to the bulk material. From equation (3.10) and using Faraday's constant (96485 C mol^{-1} per electron) the estimated theoretical capacitance for VN (65 g mol^{-1}) is 1350 Fg^{-1}, which considers 1 electron stored per mole of VN within a voltage window of 1.1V. This theoretical capacitance value is close to the experimental value of 1340 Fg^{-1} achieved by Choi et al. for the VN in aqueous KOH system [2]. Further analysis of the EXAFS region is required for understanding and characterizing the change in V local structure during charge storage.

3.6 Reference:

1. P.Pande, P.G. Rasmussen, L.T. Thompson, J. Power Sources, 207 (2012) 212

2. D. Choi, G.E. Blomgreen, P.N. Kumta, Adv. Mater. 18 (2006) 1178.

3. B.E. Conway, Electrochemical Supercapacitors, Kluwer Academics Plenum Publisher, New York, 1999.

4. J. Newman, K.E. Thomas-Alyea, Electrochemical Systems, 3rd Edition., Wiley (2004).

5. R.G. Compton, C. E. Banks, Understanding Voltammetry, World Scientific Publishing, 2007.

6. T.-C Liu, W.G. Pell, B.E. Conway, J. Electrochem. Soc. 145 (6) (1998) 1882.

7. T.-C Liu, W.G. Pell, B.E. Conway, Electrochimica Acta, 42 (23-24) (1997) 3541.

8. J. E. Penner-Hahn, X-ray Absorption Spectroscopy. eLS. 2005.

9. Ravel B, Newville M. ATHENA, ARTEMIS, HEPHAESTUS: data analysis for X-ray absorption spectroscopy using IFEFFIT. J Synchr Rad. 2005;12:537-41.

10. S.T. Oyama, The Chemistry of Transition-metal Carbides and Nitrides, Chapman and Hall Publisher, 1996.

11. Z. L. Liu, M. Meng, Y.L. Fu, M. Jiang, T.D. Hu, TD, Y.-N, Xie, T. Liu, Materials Lett. 54 (5-6), 2002, 364.

12. D. D. Pollock, Physical Properties of Materials for Engineers, Vol III, CRC Press, 1982.

13. R.Caputo, A. Alavi, Molecular Physics, Vol 101, 11, 2003,1781.

Chapter 4

Role of Solvent in Charge Storage Mechanism

4.1   Introduction

In this chapter we explore the possibility of using non-aqueous electrolytic solutions for vanadium nitride based electrochemical capacitors. VN was tested in both aqueous and non-aqueous (acetonitrile) systems containing $[(C_2H_5)_4N]OH$ as the electrolyte. We attempt to understand the role of water in the charge storage mechanism for VN.

4.2   Materials and Methods:

The electrolytic media were 0.1M tetraethylammonium hydroxide ($[(C_2H_5)_4N]OH$, 40% in H_2O Aldrich) and 0.1M tetraethylammonium tetrafluoroborate ($[(C_2H_5)_4N]BF_4$, 99%, Alfa Aesar). Acetonitrile (CH_3CN, 99.9%, Acros) was used as the organic solvent, as received. Aqueous solutions were prepared using deionized water (18 MΩ cm, Millipore Milli-Q Advantage A10).Ti-foil slurry coated macroelectrodes were prepared as described in chapter 2. Cyclic Voltammetry was performed using a three-electrode cell at a scan rate of 2mVs^{-1}. A Pt foil was used as the counter electrode and the reference electrode was Hg/HgO (0.1 mol dm^{-3} KOH, Radiometer Analytical).   Solutions were degassed with N_2 (99.998% with an oxygen trap) for at least 30 minutes prior to the experiment and a nitrogen blanket was maintained throughout.

4.3 Results and Discussion:

Figure 4.1 illustrates typical voltammograms for VN electrodes cycled in aqueous and acetonitrile-based electrolytes containing $[(C_2H_5)_4N]OH$ or $[(C_2H_5)_4N]BF_4$. The $[(C_2H_5)_4N]OH$ electrolytic species was chosen because it has good solubility in both acetonitrile and water. The $[(C_2H_5)_4N]BF_4$ electrolytic species was chosen because it is relatively redox inactive within the voltage windows used here [1] and its use eliminates OH^- from the electrolyte allowing for determination of the role of water in the charge-storage mechanism.
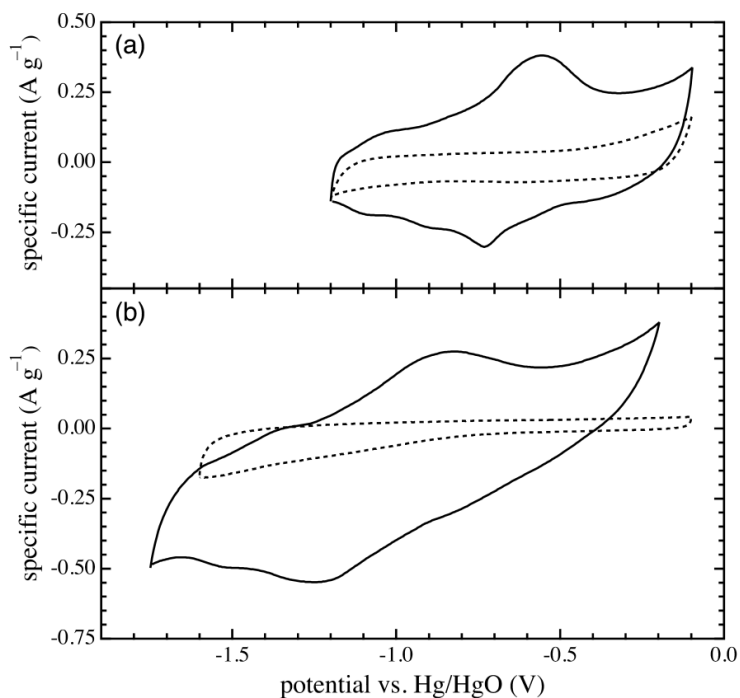
Figure 4.1 Cyclic voltammograms for VN electrodes cycled in (a) 0.1M $[(C_2H_5)_4N]OH$ in H_2O (solid line) and 0.1M $[(C_2H_5)_4N]BF_4$ in H_2O (dashed line) and (b) 0.1M $[(C_2H_5)_4N]OH$ (2.21% v/v H_2O) in CH_3CN (solid line) and 0.1M $[(C_2H_5)_4N]BF_4$ (2.21% v/v H_2O) in CH_3CN (dashed line). The scan rate was 2 mV s^{-1} and the measurements were carried out at room temperature.

In general, for the CVs of VN in $[(C_2H_5)_4N]OH$-based electrolytes, similar features are observed. In both of these CVs, redox couples are observed, which

are attributed to successive changes in the oxidation state of vanadium by adsorption of OH^- on the VN surface during cycling. A wider operating potential window was observed for the acetonitrile-based electrolyte; ~1.5 V compared to ~1.1 V in the aqueous. An increase in the potential window for the acetonitrile-based electrolyte, despite the presence of a small amount of water, suggested a suppression of the water electrolysis reaction in this solvent. This is likely due to suppression of the hydrogen evolution reaction which shows a potential shift of approximately -350 mV per decade decrease in water concentration [2], much larger than the -59 mV $decade^{-1}$ expected on Nernstian grounds. Based on the Nernst's equation the shift associated with change in water concentration from (~55M to ~1.22M) for this electrolyte would be ~97mV.

Table 4.1 Specific capacitances estimated for VN electrodes in various organic and aqueous electrolytes at a scan rate of 2 mVs^{-1}.

Electrolyte	Specific capacitance, C (F g^{-1})
0.1 M $[(C_2H_5)_4N]OH/H_2O$	201
0.1 M $[(C_2H_5)_4N]OH$ (2.21% v/v H_2O)/CH_3CN	192
0.1 M $[(C_2H_5)_4N]BF_4/H_2O$	41
0.1 M $[(C_2H_5)_4N]BF_4$(2.21% v/v H_2O)/CH_3CN	32

The voltammogramms for VN in $[(C_2H_5)_4N]BF_4$-based aqueous and organic electrolytes possessed similar features with no redox peaks observed. The specific capacitance, of the VN electrodes in the various electrolytes was estimated by integrating the area within the voltammograms, using equation (2.2). Table 4.1 lists the average specific capacitances calculated from multiple experiments in each of the electrolytes. In general, the average specific

capacitance was slightly lower in the organic electrolytes compared to the aqueous electrolytes. This difference can be reconciled based on differences in the diffuse-layer capacitances. The diffuse-layer capacitance is a function of the dielectric constant of the solvent according to [3],

$$C_d \propto \frac{\varepsilon}{\lambda} \propto \sqrt{\varepsilon} \tag{5.1}$$

where λ is the Debye length which is proportional to the square root of permittivity, ε.

Taking into account the difference between the dielectric constant of water and acetonitrile at 20 °C (80 and 37.5, respectively), one would expect the aqueous double-layer capacitance to be ~3/2 times that of the organic, as was observed here in the absence of OH⁻.

For the $[(C_2H_5)_4N]OH$-based electrolytes, an average specific capacitance of 201 F g⁻¹ was measured for VN in the aqueous electrolyte compared to 192 F g⁻¹ for the organic electrolyte. This small difference likely owes to the differences in the double-layer capacitances measured in each solvent [3,4]. If the double-layer capacitance is subtracted from the total capacitance (assuming that the double-layer and pseudocapacitive mechanisms are parallel processes), then both solvents yielded a pseudocapacitance of ~160 F g⁻¹. This suggests that the pseudocapacitive mechanism is independent of the solvent and the presence of water, and only depends on the presence of OH⁻.

The energy density, E, is a key figure of merit for electrochemical capacitors and is estimated by equation (1.1) [4].

It has been shown here that a similar capacitance is obtainable for vanadium nitride in an organic-based electrolyte compared to an aqueous electrolyte. Although an energy density cannot be calculated without charge/discharge data, comparing the potential window for the aqueous electrolyte of 1.2 V (the largest reported window for VN in aqueous electrolyte [5]), to that for the acetonitrile-based electrolyte, an increase of 0.3 V should result in approximately a 50% increase in energy density for VN in the organic electrolyte.

4.4 Conclusions

Vanadium nitride was electrochemically characterized in aqueous and organic electrolytes. An average specific capacitance of 201 F g^{-1} was measured for the VN material for both aqueous and acetonitrile electrolytes. From experiments with [(C$_2$H$_5$)$_4$N]BF$_4$-based electrolytes, it was determined that water does not play a role in the pseudocapacitive charge-storage mechanism. A potential window of ~1.5 V was observed in the acetonitrile-based electrolyte. For the same measured capacitance, an increase in voltage window of 0.3 V for VN in the organic electrolyte investigated here, compared to typical voltage windows for the aqueous electrolytes, translates into an increase in energy density of ~56%. This result is of interest for the development of higher-energy-density vanadium nitride-based electrochemical capacitors.

4.5 References

1. M. Ue, K. Ida, S. Mori, J. Electrochem. Soc., 141, 1994, 2989.

2. Y. Tomita, S. Teruya, O. Koga, Y. Hori, J. Electrochem. Soc., 147, 2000, 4164.

3. J. Newman, K.E. Thomas-Alyea, Electrochemical Systems, 3rd Edition., Wiley (2004).

4. B.E. Conway, Electrochemical Supercapacitors; Kluwer Academic/ Plenum Publishers, (1999).

5. P.Pande, P.G. Rasmussen, L.T. Thompson, J. Power Sources, 207 (2012) 212.

Chapter 5

Summary, Conclusions, Limitations and Future Work

5.1   Summary and Conclusions

The primary goal of research described in this dissertation was to define charge storage reactions for early transition metal nitrides electrode materials for electrochemical capacitors. Nitrides and carbides of Mo, V and W were synthesized by temperature-programmed reaction of inexpensive oxides. Physical properties including the phase purity and surface area were characterized using XRD and N_2 physisorption, respectively. Electrochemical properties of the materials including the stability and capacitance in aqueous H_2SO_4 and KOH were characterized using cyclic voltammetry. VN in KOH (1.1V, 210 Fg^{-1}) and Mo_2N in H_2SO_4 (0.8V, 346 Fg^{-1}) were identified as the most promising systems were identified on the basis of their wide stability window and gravimetric capacitance. Charge storage mechanisms were proposed for these systems .

Electrochemical characterization results showed that Mo_2N and W_2C were stable in aqueous H_2SO_4, while VN, VC and W_2N were stable in aqueous KOH. Mo_2C was unstable in both aqueous H_2SO_4 and KOH. Mo_2N in aqueous H_2SO_4 with a voltage window of 0.8V and capacitance of 346 Fg^{-1} along with VN in aqueous KOH with a voltage window of 1.1V and gravimetric capacitance of 210

Fg^{-1} were found to be the most promising systems. For Mo$_2$N in aqueous H$_2$SO$_4$, the gravimetric capacitance of 346 Fg^{-1} was the highest reported value yet [1].

Charge storage mechanisms for Mo$_2$N in H$_2$SO$_4$ and VN in KOH were established by dividing the reaction equation into its components: electrolyte ions, charge transferred and the changes in the electrode material. A series of electrolyte ion isolation and substitution experiments suggested that H$^+$ was active for charge storage in Mo$_2$N in H$_2$SO$_4$, while OH$^-$ was active for charge storage in VN in KOH. The amount of charge transferred and the active species reacted was determined by establishing the relationship between the rest potential of the system to the active species concentration. The slope of this linear relation, according to the Nernst equation, was proportional to the coefficient of the concentration term [2]. These results indicated that for Mo$_2$N in H$_2$SO$_4$, for every proton reacted approximately 2 electrons are stored. For VN on KOH, one electron and 2 hydroxyls were involved in the reaction.

In situ XAS experiments were used to define the changes in the electrode material chemical states. There appeared to be approximately 1 electron change in oxidation state per Mo in Mo$_2$N and approximately 1 electron change in V oxidation state during charge storage in VN. Together the results suggested the following charge storage reactions:

$$\text{Mo}^{\delta}{}_2\text{N} + 2\text{H}^+ + 4\text{e}^- \leftrightarrow \text{Mo}^{\delta\,-1}{}_2\text{N}(\text{H}_{\text{abs}})_2 \tag{3.7}$$

$$\text{V}^{\delta}\text{N} + 2\text{OH}^- \leftrightarrow \text{V}^{\delta\,-1}\text{N} + \text{H}_2\text{O}_2 + \text{e}^- \tag{3.10}$$
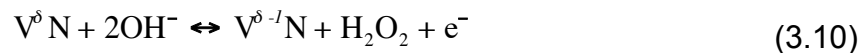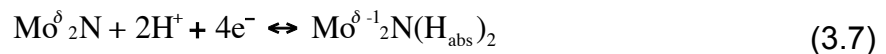
For Mo_2N in H_2SO_4, we believe the H occupied vacant tetrahedral sites in the *fcc* lattice. Theoretical capacitance estimates from these reactions were 2340 Fg^{-1} for Mo_2N and 1350 Fg^{-1} for VN, based on Faraday's law [2].

To identify the role of the electrolyte solvent, VN was evaluated in aqueous and organic (acetonitrile) systems. The $[(C_2H_5)_4N]OH$ salt was used as the electrolyte due to its good solubility in aqueous and organic solvent. The results from this study indicated, that water does not play a role in pseudocapacitive charge storage, as both aqueous and organic systems had an average capacitance of 200 Fg^{-1}. Additionally, VN in $[(C_2H_5)_4N]OH$ in acetonitrile had a wider stability window of 1.5V compared to 1.1 V in water. This increase in the voltage window would translate to an energy density increase of ~50%.

5.2 Limitations of Current Research and Future Work

5.2.1 Limitations

The research presented in this dissertation provides insights about the charge storage mechanism of transition metal nitrides. The results from the various experimental techniques used, identified several key aspects of the charge storage mechanism. As there are certain limitations associated with these techniques, the areas listed below require further investigation.

5.2.1.1 Capacitance Measurement

Cyclic voltammetry was employed for capacitance measurement. The capacitance values were estimated at $2mVs^{-1}$, as shown in chapter 2. These values provided an estimate of the charge storage capabilities of the materials,

however, as the measurements were performed only at one scan rate, this method was not able to distinguish between the double layer and pseudocapacitive contribution. In order to estimate pseudocapacitance versus double layer contribution, capacitance measurements need to be performed at a wide range of scan rates [4,6,7]. Double layer capacitance of a material is thought to be independent of scan rates, however, depending upon the charge storage mechanism, pseudocapacitance varies with scan rate. For Ru_2O in aqueous H_2SO_4 system at high scan rates (500-1000 mVs^{-1}) only the double layer mechanism contributes towards charge storage [7]. Sugimoto et al. utilized this procedure and subtracted the double layer capacitance obtained at high scan rates to estimate pseudocapacitive charge storage [7]. Similar experimental procedure could be employed to distinguish the contribution of double layer and pseudocapacitive charge storage for transition metal nitrides and carbides.

5.2.1.2 Surface versus Bulk material Contribution to Charge Storage and the Role of the Passivation Layer

In situ XAS was employed to identify the changes in the material during charge storage. As XAS was used in the transmission mode to characterize the electrode materials, only average changes in the oxidation state and the local structure of the material were detected. The discrete contributions of the surface layer versus the bulk material could not be identified. Additionally, the role of the oxygen-rich surface passivation layer was not well understood.

The surface involvement in the charge storage mechanism could be understood by performing *in situ* XAS experiments using thin-film electrodes.

Thin-film early transition metal nitride or carbide electrodes can be developed using techniques like atomic layer deposition, chemical vapor deposition or magnetron sputtering on a metal substrate or on conductive glass [3, 4]. *In situ* XAS experiments in the fluorescence mode would be ideal for thinnest films with nearly atomic scale thickness (~ 1 nm- 2 nm) to avoid signal attenuation by the substrate. Characterizing films with varying thickness would provide insights regarding contribution from the surface layer compared to the bulk-like atoms in "thick-film" electrode. This techniques would also shed light on the role of oxygen-rich passivation layer in the charge storage mechanism.

Another method for characterizing the surface contribution to charge storage could be done by performing a quick *in situ* XAS experiment in conjunction with AC modulation (~ 5 mV-10 mV) of the applied DC voltage to the electrode at various frequencies [5]. It is anticipated that at high frequencies (~100000 Hz- 10000 Hz) only the surface of the electrode will be active for charge storage and in the low frequency regime (1000 Hz to 0.01 Hz) the bulk material will be active to charge storage. The frequency of the XAS data collection will have to be matched or should be higher than the frequency of the electrochemical AC modulation. Prior to the *in situ* quick XAS experiment the frequency response of the electrode-electrolyte system should be modeled by using techniques like electrochemical impedance spectroscopy.

5.2.2 Extension of Current Research

The identification of changes in the VN local structure during charge storage would be useful in establishing the extent of their interaction with VN and

their contribution to the charge storage mechanism. This could be studied by performing *in situ* XAS experiment as was done for Mo_2N. The XAS data would be collected in the EXAFS region up to 1000 eV beyond the V K-edge (5465 eV). The analysis of the EXAFS region of these results would show if ligand substitution interactions occur during VN charge storage.

In addition to VN in KOH and Mo_2N in H_2SO_4, W_2C in H_2SO_4 (0.8V, 494 Fcm^{-2}) was another promising system based on its stable operating voltage and areal capacitance. The cyclic voltammograms for W_2C in H_2SO_4 (figure 2.11) had redox couples, which suggested series of oxidation state changes. The techniques described in this dissertation (Chapter 3) could be applied to understand the charge transfer mechanism of W_2C in H_2SO_4.

5.2.3 Prototype development

The focus of research described in this dissertation was characterization of charge storage for selected early transition metal nitride based electrochemical capacitor electrodes. In order to use these materials in a device there are several aspects that require careful consideration including: (1) electrolyte concentration, (2) electrode surface area, and (3) counter electrode [6].

5.2.3.1 *Effect of Electrolyte Concentration*

Electrolyte concentration is an important factor with regard to double -layer capacitors. Double layer capacitance varies directly with the square root ionic strength, which is a function of electrolyte concentration (within the bounds of dilute solution theory) [6,8],

$$C_{dl} = \frac{\varepsilon}{\sqrt{\dfrac{\varepsilon RT}{2F^2 I}}}$$ (5.1)

here, C_{dl} is the double layer capacitance, ε is the permittivity of the electrolyte, R is the universal gas constant, T is the temperature, F is Faraday's constant and I is the ionic strength of the solution. In concentrated solutions, after the initial increase in capacitance double layer capacitance plateaus and does not increase any further [6]. It would be interesting to study the effect of electrolyte concentration on pseudocapacitance for the early transition-metal-nitrides and carbides. This study would help identify the optimum electrolyte concentration to achieve high capacitances.

5.2.3.2 Effect of Electrode Surface Area

In this study the surface area of the materials tested were not varied. For double layer capacitors, the capacitance of the electrode proportional to the accessible electrode surface area [6]. However in pseudocapacitive charge storage, the capacitance can be a function of (1) the extent of adsorption of a species on the surface of the electrode or (2) extent of fractional absorption of a species into the lattice of the electrode material or (3) extent of redox reactions on the electrode surface [6]. It would be reasonable to hypothesize that if the availability of the surface sites for these processes is increased, the capacitance of the material would increase. The effect of electrochemically accessible surface area to pseudocapacitance charge storage would be interesting to look at.

5.2.3.3 Counter Electrode

Electrochemical capacitors can be defined as symmetric or asymmetric depending on the counter electrode chosen [6]. In symmetric electrochemical capacitors, same material is used on both sides as negative and positive electrode [6]. This is common in double-layer capacitors [9,10]. For pseudocapacitors there two types of arrangements have been observed: (1) symmetric: same material is used as both negative and positive electrode and (2) asymmetric: another material is used as the counter electrode, this material could be a double-layer based material like high surface area carbon, a different material active for pseudocapacitive charge storage for example, early transition metal nitrides could be paired with transition metal oxides showing pseudocapacitive charge storage or it could be an electrode materials used in batteries [6,11].

While pairing negative and positive electrode the following factors must be considered:

- The stable operating voltage of each electrode must complement each other
- Mass ratio: The capacitance of the cell is given by equation (5.2) [12]

$$\frac{1}{C_-} + \frac{1}{C_+} = \frac{1}{C_{Cell}} \tag{5.2}$$

Where C_- and C_+ are the capacitances of the negative and positive electrode respectively. Thus the electrode with lowest capacitance would dominate the capacitance of the cell. During charge storage the negative

93

and positive electrode are equally charged such that $Q_- = Q_+$ [12]. In order to maximize the utilization of the available voltage window it is important to optimize active mass ratio electrodes as shown by the relationships in equations (5.3) and (5.4) [12]:

$$\hat{C}_- m_- V_- = \hat{C}_+ m_+ V_+ \qquad (5.3)$$

$$\frac{m_-}{m_+} = \frac{\hat{C}_+ V_+}{\hat{C}_- V_-} \qquad (5.4)$$

Here, $\hat{C}_+$ and $\hat{C}_-$ are the specific gravimetric capacitance of the positive and negative electrodes respectively. V_+ and V_- are the voltage windows and m_+ and m_- are the masses of the active materials for the positive and negative electrodes respectively.
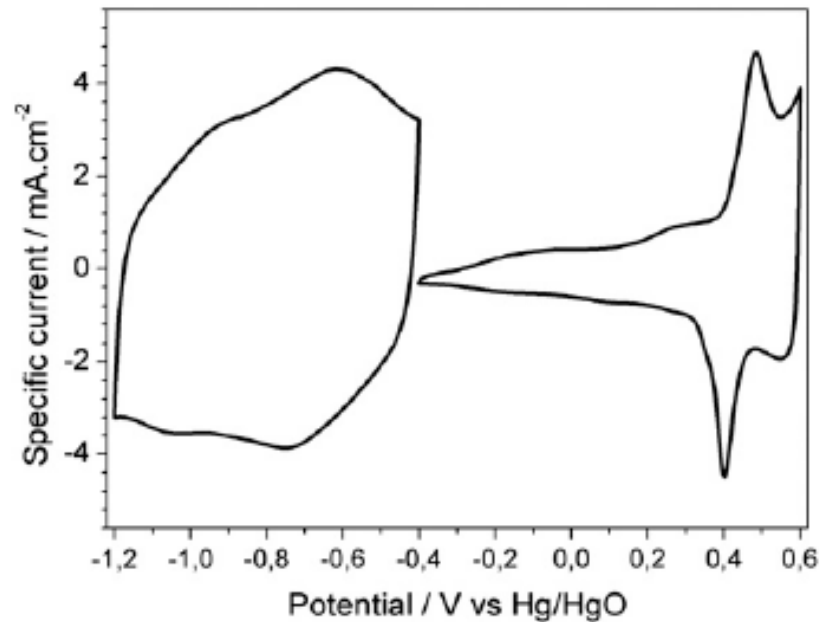

Figure 5.1: Cyclic voltammograms at 200 mV s−1 of sputtered VN thin film (left side) and electroplated NiO thin film (right side) at a scan rate of 200 mV s−1 in 1 MKOH electrolyte. Taken from [11].

Based on these considerations, high surface area carbon electrodes could be suitable as counter electrode for both VN in KOH and Mo_2N in H_2SO_4 systems, as carbon is known to be stable in both acidic and basic media and can have capacitance ~125 Fg^{-1} [9,10]. Additionally, NiO electrodes from the Ni-metal hydride batteries could be suitable as positive electrodes with VN as negative electrode in an aqueous KOH system [11]. Figure 5.1, shows cyclic voltammograms of VN and NiO thin-films, the voltage windows of these systems are complimentary. Also, NiO has been used in alkaline batteries [11]. For Mo_2N in H_2SO_4, PbO_2 electrodes found in lead acid batteries could be suitable, due to their high capacitance and complimentary stability windows. PbO_2 would be the positive electrode, while Mo_2N would be the negative electrode [14].

The findings presented in this dissertation, provide insights into the chemistries of early transition metal nitrides as electrochemical capacitor electrodes. The results and the direction provided here would be useful in developing novel chemistries for future electrochemical capacitors.

References

1. P.Pande, P.G. Rasmussen, L.T. Thompson, J. Power Sources, 207 (2012) 212.

2. R.G. Compton, C. E. Banks, Understanding Voltammetry, World Scientific Publishing, 2007

3. V. V. Atuchin_, T. Khasanov, V. A. Kochubey, L. D. Pokrovsky, Int. J. Mod. Phys. B, Vol. 23, No. 23 (2009) 4817.

4. T.-C Liu, W.G. Pell, B.E. Conway, J. Electrochem. Soc. 145 (6) (1998) 1882.

5. X. Yu, Q, Wang, Y. Zhou, H. Li, X.-Q. Yang, K.-W. Nam, S. N. Ehrlich, S. Khalid, Y. S. Meng, Chem. Commun., Vol 48, (2012) 11537.

6. B.E. Conway, Electrochemical Supercapacitors; Kluwer Academic/ Plenum Publishers,1999.

7. W. Sugimoto, T. Kizaki, K. Yokoshima, Y. Murakami, T. Takasu, Electrochimica Acta, Vol 49 (2004) 313.

8. J. Newman, K.E. Thomas-Alyea, Electrochemical Systems, 3rd Edition., Wiley (2004).

9. P. Simon, Y. Gogotsi, Nature Materials, 7 (2008), 845-854.

10. Y. Zhu, S. Murali, M. D. Stoller, K. J. Ganesh, W. Cai, P. J. Ferreira, A. Pirkle, R. M. Wallace, K. A. Cychosz,3 M. Thommes, D. Su, E. A. Stach, R. S. Ruoff, Science, 332, (2011) 1537.

11. E. Eustache, R. Frappier, R. Lucio-Porto, S. Bouhtiyya, J. F. Pierson, T. Brousse, Electrchem. Comm. 28 (2013) 104.

12. V. Khomenko, E. Raymundo-Piñero, F. B´eguin, J. Power Sources 153 (2006) 183.

13. N.W. Duffy, W. Baldsing, A.G. Pandolfo, Electrochimica Acta 54, 2008, 535.

14. H. Karami, B. Kafi, S. N. Mortazavi, Int. J. Electrochem. Sci., Vol 4 (2009), 414.

Appendix

Figures A.1 and A.2 show results of long term cycling experiments for Mo$_2$N in 0.5M H$_2$SO$_4$ and VN in 1M KOH for 700 cycles, respectively. CV was performed in a three-electrode cell using macroelectrodes as described in chapter 2.
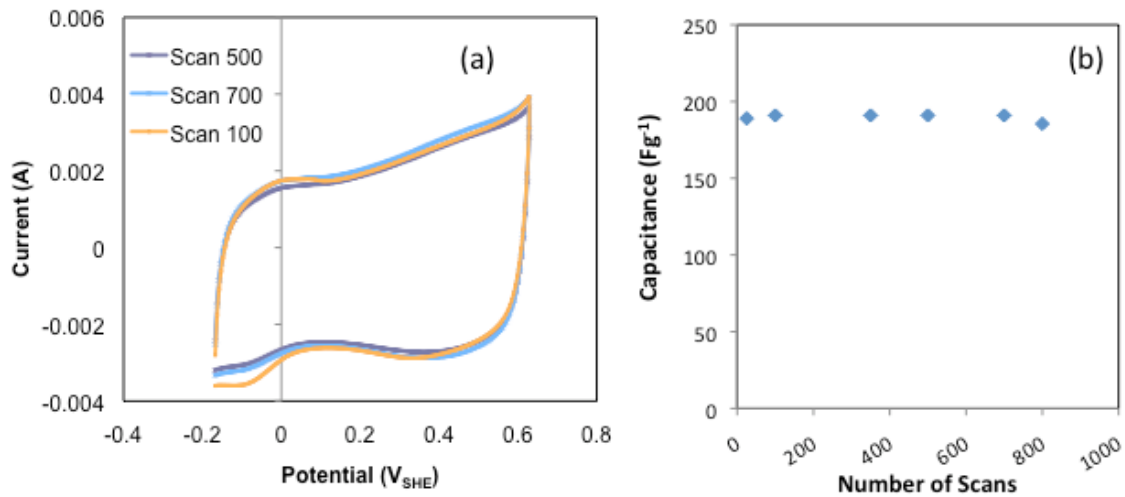

Figure A.1 (a) Cyclic Voltammograms of Mo$_2$N in 0.5M H$_2$SO$_4$ at a scan rate of 12.5 mVs^{-1} at room temperature for 700 scans/cycles. N$_2$ blanket was maintained throughout the experiment. (b) Capacitance measured for various scans.
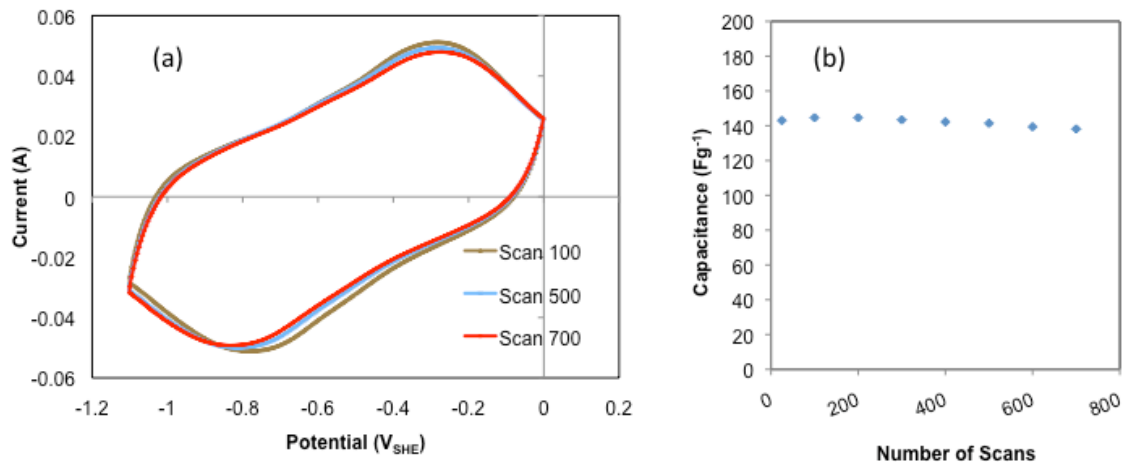
Figure A.2 (a) Cyclic Voltammograms of VN in 0.1M KOH at a scan rate of 50 mVs^{-1} at room temperature. N$_2$ blanket was maintained throughout the experiment. (b) Capacitance measured for various scans.

Figures A.3 and A.4 show Raman spectra collected for Mo$_2$N and VN, respectively. A 532 nm laser source with Raman detector (Dimension P1 Raman system, Lambda Solutions Inc.) was used to perform the characterization. Samples were prepared by depositing 10 µl of slurry prepared by dispersing 5 mg Mo$_2$N or VN in 5 ml ethanol (sonicated for 20 minutes) on an alumina coated glass substrate (1 cm X 1 cm). The slurry was dried at room temperature for 30 minutes. The Raman spectra did not show any peaks, suggesting that Mo$_2$N and VN did not show discrete vibrational modes for V-N or Mo-N bonds.
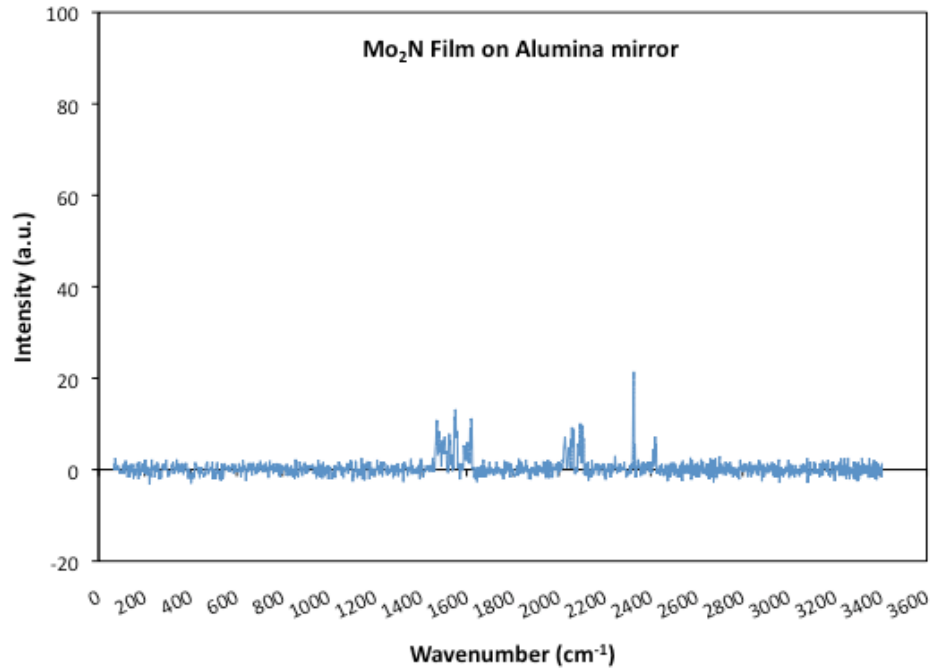
Figure A.3 Raman spectra collected for Mo_2N deposited on an alumina coated glass substrate (1cm X 1cm) using a 532 nm laser source.
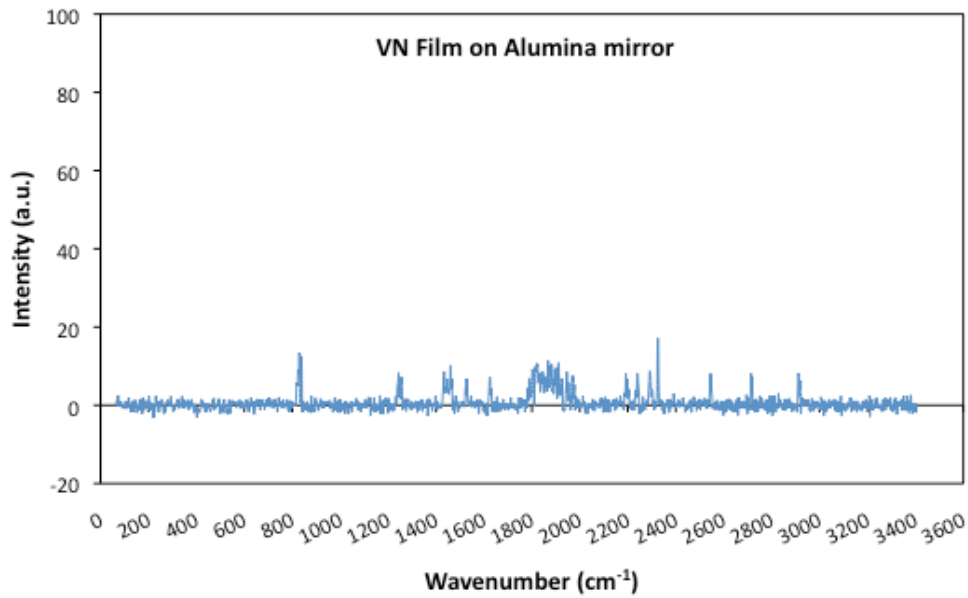

Figure A.4 Raman spectra collected for VN deposited on an alumina coated glass substrate (1cm X 1cm) using a 532 nm laser source.